Master's Thesis

Development of an Optically Detected Magnetic Resonance Spectrometer

Milán Negyedi

Thesis leader: Ferenc Simon
Professor
BME Physical Institute
Department of Physics

Budapest University of Economy

2014

Diplomamunka feladat a Fizikus mesterképzési (MSc) szak hallgatói számára

A hallgató neve:	**Negyedi Milán János**	szakiránya:	**alkalmazott fizika**
A diplomamunkát gondozó (a záróvizsgát szervező) tanszék:			**Atomfizika Tanszék**

A diplomamunka készítésének helye:	**BME Fizika tanszék**		
A témavezető neve:	**Simon Ferenc**	A konzulens neve: (külső témavezető esetén kijelölt tanszéki munkatárs)	
– munkahelye:			
– beosztása:	**Egyetemi tanár**	– beosztása:	
– e-mail címe:	**simon@esr.phy.bme.hu**	– e-mail címe:	

A diplomamunka címe:	**Optikailag detektált mágneses rezonancia spektrométer fejlesztése**	azonosítója: **DM-2013-62**

A téma rövid leírása, a megoldandó legfontosabb feladatok felsorolása:

Az optikailag detektált mágneses rezonancia (ODMR) alkalmas molekulák és molekuláris szilárdtestek elektronikus és optoelektronikai tulajdonságainak mérésére. A módszer az optikai detektálás érzékenységét kombinálja a mágneses rezonancia nagy energiafelbontásával és utóbbi módszer érzékenységével a molekuláris szerkezetre és a molekulák lokális környezetére. Emellett lehetővé teszi olyan optikai átmenetek vizsgálatát, melyek a hagyományos optikai gerjesztésekkel nem elérhetőek és így nem vizsgálhatóak valamint optikai és mágneses rezonanciás kereszteffektusok, relaxációs mechanizmusok vizsgálatát. Technikailag, az ODMR berendezés kifejlesztése az elektron spin rezonancia és optikai spektrométerek kombinálását jelenti. A jelentkező számára a gyakorlati tennivalók: a nemrégiben beszerzett optikai spektrométer vezérlő programjának módosítása és integrálása, az optikai összeállítás optimálása Raman és fluoreszcens mérésekre, a fénydetektorok mérési tartományának kimérése, különös tekintettel az alacsony fotonszámú esetre, az optikai és ESR spektrométer integrálása, valamint demonstratív ODMR mérések elvégzése. Az ideális jelentkező jó gyakorlati érzékkel rendelkezik, alapos, türelmes és óvatos munkavégzésre képes (ez elengedhetetlen az optikai rendszerek beállításához) valamint képes a munka érthető összefoglalására.

A feladat kiadásának időpontja: **2013-02-05**

Témavezető vagy tanszéki konzulens aláírása:	A diplomamunka témakiírását jóváhagyom (tanszékvezető aláírása):

Alulírott Negyedi Milán János, a Budapesti Műszaki és Gazdaságtudományi Egyetem fizikus MSc szakos hallgatója kijelentem, hogy ezt a diplomamunkát meg nem engedett segédeszközök nélkül, önállóan, a témavezető irányításával készítettem, és csak a megadott forrásokat használtam fel. Minden olyan részt, melyet szó szerint, vagy azonos értelemben, de átfogalmazva más forrásból vettem, a forrás megadásával jelöltem.
Budapest, 2014-05-22

aláírás

Contents

Thanks

Szeretném megköszönni témavezetőmek, Simon Ferencnek fáradhatatlan munkáját, példamutatását és legfőképpen türelmét. Nélküle ez a dolgozat nem készült volna el. Emellett köszönöm a Fizika tanszék munkatársainak, Horváth Bélának és Bacsa Sándornak a méréseinkhez szükséges számos különleges alkatrész elkészítését. Munkájuk nélkül a kísérleteket szigetelőszalag tartotta volna össze. Köszönöm Palotás Juliannának, Dzsaber Száminak és Gyüre Balázsnak, hogy a mérések során segítségemre voltak. Köszönet Fortágh Józsefnek a rendkívül motiváló nyári gyakorlati lehetőségért a Tübingeni Egyetemen. Végezetül köszönöm a családomnak, hogy végig mellettem álltak, és Rékának egyszerűen csak azt, hogy létezik.

I would like to thank Philip Rohringer and Thomas Pichler for their help in preparing the samples and with stimulating discussion of the results and for their hospitality during our visit to Vienna. Financial support by the European Research Council Grant Nr. ERC-259374-Sylo is acknowledged.

Chapter 1

Introduction and motivations

The photophysics of single-wall carbon nanotubes (SWCNTs) is intensively studied due to their potential applications in light harvesting and optoelectronics. The excited states of SWCNTs form strongly bound electron-hole pairs, which are known as excitons. Of such excitons, only those with a singlet spin symmetry are spin-allowed and are useful for applications but they can form triplet excitonic states with a low probability, a process known as intersystem crossing. Much as their formation probability is low, the triplet excitons are long-living, their decay also being a slow process, they therefore accumulate which hinders the application of SWCNTs either for light harvesting or for the inverse process of light generation. It is therefore crucial to gain information about the triplet exciton energy level structure, magnetic properties, and decay dynamics but yet little is known about these.

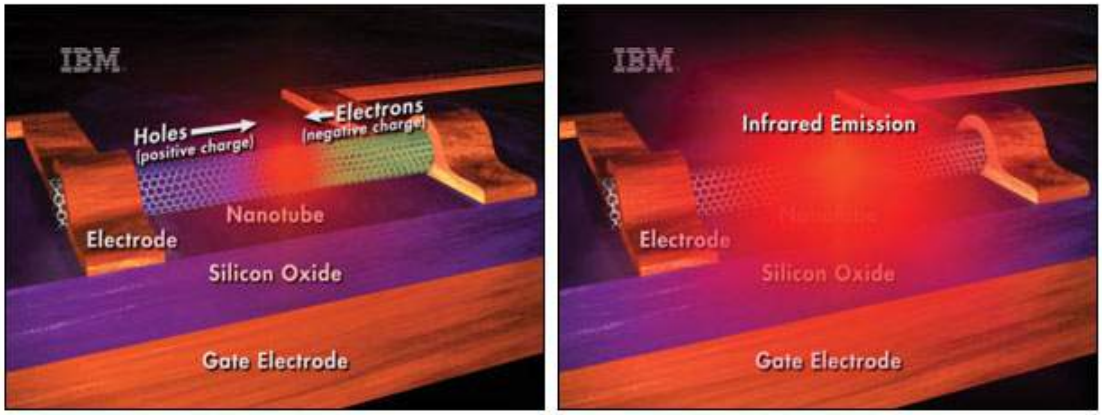

Figure 1.1: A nanotube-based light-emitting transistor from IBM. Source: [1]

.

Here, we present the development of an optically detected magnetic resonance (ODMR) spectrometer which is designed to observe the aforementioned triplet states of nanotubes. With the spectrometer, we can observe the following:

- bounding energy of the triplet excitons

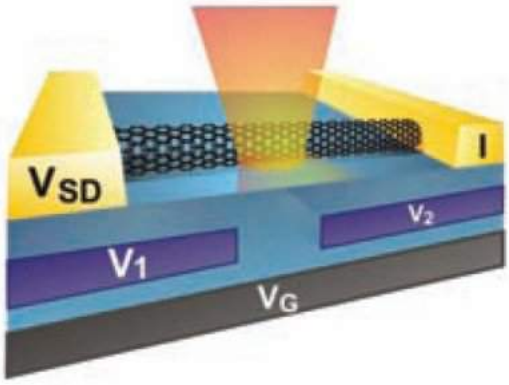

Figure 1.2: Concept of a nanotube based solar cell by Cornell. Source: [2]

.

- details of the magnetic energy structure of the nanotubes
- investigate the decay times of nanotubes with different chirality.

ODMR spectrometers have been developed in various laboratories [3]. These usually operate with a single laser excitation, emission in the visible without wavelength resolution. The specific nature of SWCNTs, i.e. narrow narrow emission and excitation profiles and the fact that no homogeneous nanotube sample is available, requires the use of tunable laser excitation and spectral resolution of the emitted light in the near infrared. These requirements presented important challenges for our development. Beside this, compared to commercial photoluminescent (PL) spectrometers, it also has the following advantages:

- Laser excitation, which has about 100-times the optical intensity of the Xe lamps commonly used in PL spectrometers.
- A light gathering optical system optimized for high performance. Conventional PL spectrometers have a light gathering capability a factor of ten worse.
- An interferometric edge filter for filtering out unwanted light entering the spectrometer. At least an order of magnitude better than those used in commercial PL spectrometers.

In this thesis, we describe the development of this spectrometer, the challenges encountered during our work, and the results obtained by its use.

Chapter 2

Theoretical background

2.1 Carbon nanotubes

2.1.1 History

The discovery of carbon nanotubes is generally attributed by the scientific audience to Sumio Iijima [4], who published his results in Nature (1991). This was the article that drew the interest of the community to this family of materials. The reason why it succeeded in calling attention to nanotubes is the groundbreaking role that the researcher played both in the fields of nanomaterials and high resolution electron-microscopy.

However, the situation is not entirely so clear. First, an important distinction is to be made between single-walled (SWCNT) and multi-walled (MWCNT) carbon nanotubes. The history of MWCNT-s goes back as early as the end of the 19th century (1889) when they were proposed by Hughes and Chambers as an alternate filament to be used in light bulbs. Back then, the conventional optical microscopes did not have the needed resolution to observe the inner structure of these filaments. In the 1950s, with the proliferation of the commercial electron microscopes, the first real description of nanotubes were made by Radushkevich and Lukyanovich. They described hollow carbon filaments of 50 nm diameter. These were MWCNT-s, probably about 15-20 concentric sheets of graphene.

In the following 20 years, over 10 articles were published describing the structure of these hollow tubes. But these results remained "hidden" until Iijima's article in 1991, after which carbon nanotubes first gained widespread attention. In the case of SWCNT-s, the facts are more straightforward, Iijima and Ichihashi [5], and Bethune *et al.* [6] reported their findings in the same issue of Nature (1993). The reasons why the previous results were mostly "hidden" before the 1991 article are the following. First, previously the nanotubes were mostly investigated from an applied point of view, to stop them from being created in the steel and oil industry, or in the coolant systems of graphite moderated nuclear reactors. Because of these, these articles did not enter the "mainstream" of solid state physics and materials science. Second, the scientific community did not have the necessary resources (experimental equipment, theoretical background and free mental capacity) to be able to recognize the importance of the discoveries until 1991.

2.1.2 Fundamentals of carbon nanotubes

Geometry

The geometry of SWCNT-s is best understood if we picture it by "rolling up" an imaginary sheet of graphene. We designate two carbon atoms as the end points of a vector, then roll up the sheet such as the length of this vector will become the circumference of the tube. This is a so-called (n, m) nanotube, where n and m represent the coordinates of the selected vector(on the graphene basis vectors), which is called *chirality* or *Hamada vector*. This is depicted in Figure 2.1.

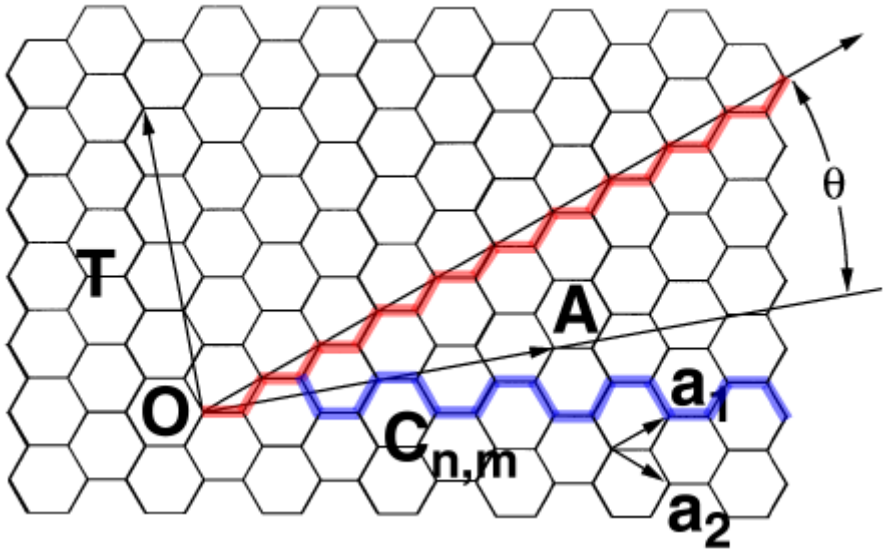

Figure 2.1: The geometry of a graphene sheet. The primitive cell vectors are denoted by $\mathbf{a_1}, \mathbf{a_2}$. The blue line is the Hamada vector for an *armchair*, the red is for a *zig-zag* tube. Source: [7]

.

At the end of the nanotubes, we observe special shapes in specific cases of the chirality vector. The two such cases are: $n{=}m$, which is called *armchair*, and the $m{=}0$ case, the so-called *zig-zag* nanotube. Apart from these two special cases, all nanotubes are *chiral*, meaning they have a non-superposable mirror image.

There is a direct relationship between the chirality vector and the diameter of the tubes. For nanotube with (n, m) chirality, the diameter is as follows:

$$d = \frac{a_0\sqrt{n^2 + m^2 + nm}}{\pi} \tag{2.1}$$

where $a_0 = 0.2461$ nm is the length of the carbon-carbon bond in CNT-s. When growing SWCNT-s catalytically, the distribution of SWCNT abundance was found to follow well a Gaussian function around a mean value with a given variance. Obviously, the SWCNT diameters do not form an evenly spaced arithmetic series due to the geometrical constraints. An example of this distribution is shown in Figure 2.2.

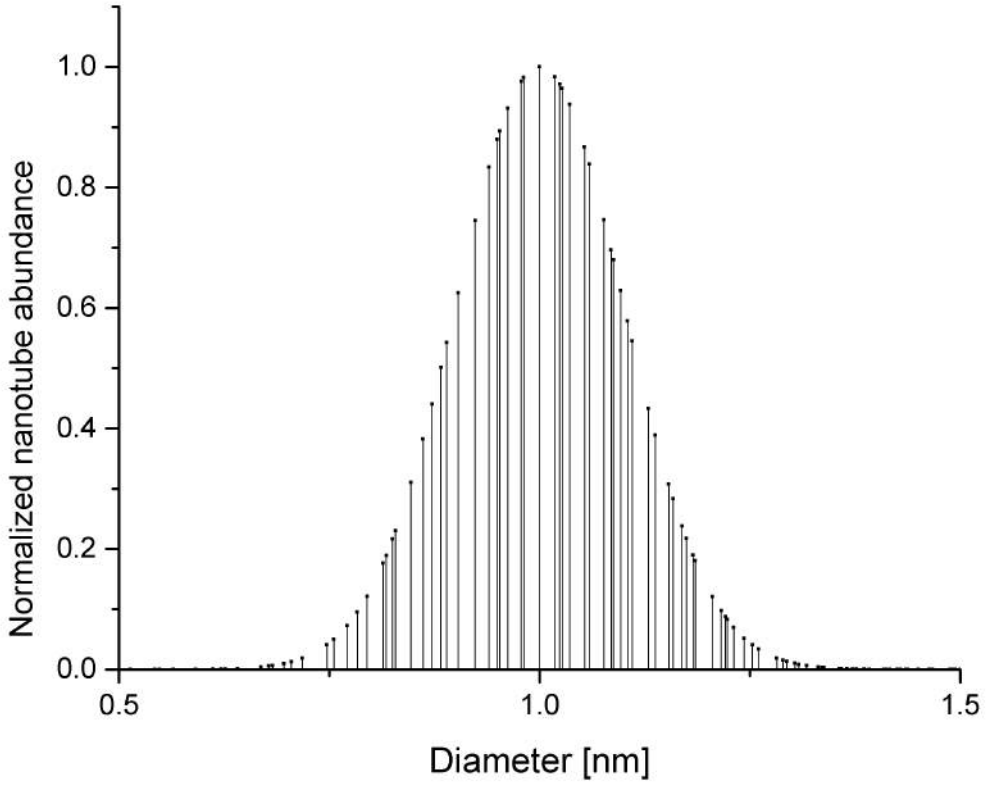

Figure 2.2: The normalized abundance of the nanotubes in a real sample with a distribution around 1 nm and a variance of 0.1 nm.

Synthesis

Very similar synthesis methods are used for SWCNTs and MWCNTs with one important difference: SWCNTs are known to be grown exclusively in the presence of catalysts which are most usually transition metal (e.g. Ni, Co, Fe) or rare earth metal (e.g. Y) elements. At present, five methods are used to manufacture :

- Pyrolysis
  Some kind of carbon-hydrogen is pumped through a tube into a furnace (by some kind of carrier gas). It vaporizes, then transfers to a second, hotter furnace, where pyrolysis takes place. Depending on the desired parameters of the tubes, temperature is varied between 600-900 degrees Celsius. After the pyrolysis phase finishes, the gas flow is shut off, temperature is raised and the annealing happens on the wall of the furnace.

- Arc discharge
  A DC current discharge is maintained between two carbon electrodes in an argon atmosphere. The nanotubes grow on the surface of the negative electrode. This was the method used by Iijima to produce the first SWCNT-s.

- Laser ablation

This technique uses a high-temperature reactor, where graphite is vaporised by a pulsed laser. Nanotubes are formed on the cooler surfaces by the condensing carbon. This method yields SWCNT-s, with a diameter distribution controlled by the reaction temperature. The first fullerenes were also made by this method.

- Plasma torch
  A flammable gas mixture including some sort of carbon-containing gas is introduced into a microwave plasma torch. The fumes exiting this torch contain SWCNT-s and other contaminating materials, which can be filtered out.

- Chemical Vapor Deposition
  A substrate covered with catalyst particles is used. The diameter of these metal particles controls the tube diameter distribution. The nanotubes are formed when a process gas and a carbon-containing gas are introduced into the reactor. The tubes grow on the edges of the catalyst particles. A version of this process, *HiPco* (High pressure CO conversion), was used in synthesizing the samples used by us.

The most distinctive characteristic of carbon nanotubes, be they single-, or multi-walled, is the huge length-to-diameter ratio (up to a hundred million in extreme cases), making them quasi one-dimensional. Another interesting property of CNT-s is that every carbon atom has the same bonding state, almost sp^2, like in graphite and graphene. These properties give carbon nanotubes interesting mechanical and electric properties. In the following of this thesis, the discussion is focused on SWCNTs to which we shall refer to as nanotubes (CNTs) for brevity.

2.1.3 Electrical and optical properties of carbon nanotubes

CNT-s also display interesting electrical properties originating in their quasi one-dimensonality. We find quasi-continous electron dispersion in the k-space direction equivalent to the length of the tube in real space and discrete states along the other two axes. The simplest, tight-binding model based approximation yields a simple rule for determining if a nanotube with a given chirality is metallic or not. The (n,m) nanotube is metallic, if $(n-m)\text{mod}3 = 0$, and is insulating with a few eV-s of band gap otherwise. Because of the quasi one-dimensionality of the geometry of the tubes, we find van Hove singularities in the density of states of the nanotubes. As shown In Figure 2.3, the two CNT-s have almost identical diameters, yet their band structure is very different.
Optical transitions in the DOS (between the singularities) are governed by selection rules derived from the unique properties of the nanotubes. The van Hove singularities can be numbered starting from the Fermi energy. The corresponding optical transitions, e.g. from the ith Van Hove singularity in the valence band to the jth van Hove singularity in the conduction band are labeled E_{ij}. We are now considering only one-photon processes. A single photon will change the z component of the angular momentum (m) by $\Delta m = 0, \pm 1$. Ordinarily, one-photon processes occurring on the tube can be classified as follows:

- Light is polarized along the axis of the tube. Only transitions between states corresponding to the same z component of the angular momentum (m) are allowed. Thus, only E_{ii} type transitions can happen.

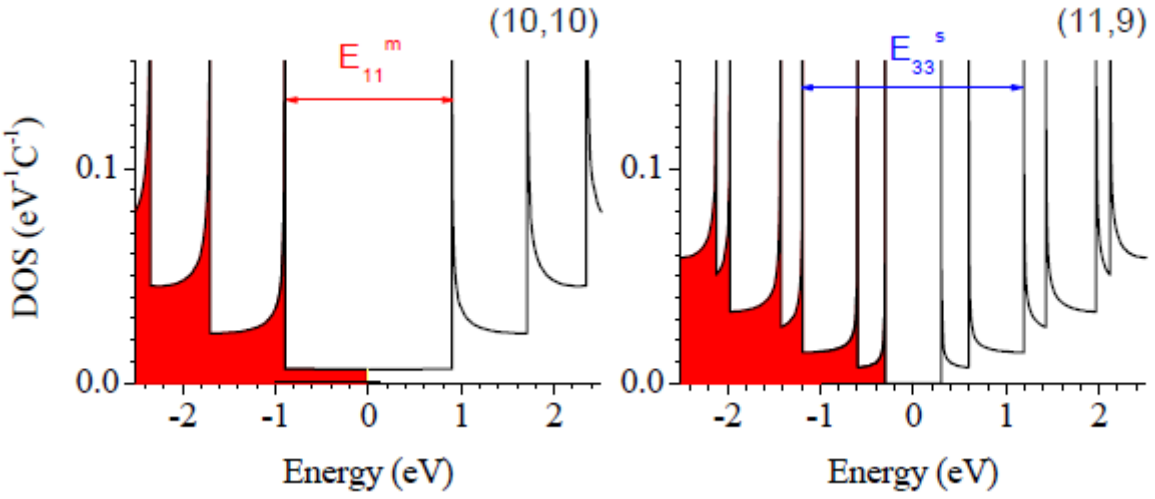

Figure 2.3: The density of states of the (10,10) metallic and the (11,9) insulating nanotube. Source: [7]. Note that there is a continuum of states between the van Hove singularities for the metallic nanotubes, whereas there is a gap for the semiconducting ones.

- Light is polarized in some direction perpendicular to the axis of the tube. This way, only transitions with a change in m ($\Delta m = \pm 1$) are allowed. This would correspond to the $E_{ii\pm1}$ types of transitions. However, due to the so-called antenna effect, these transitions are much weaker than the symmetric ones. This effect works the following way: when an external **E** field perpendicular to its axis is applied to the nanotube, the field induces charges on the tube walls. These, in turn, reduce the strength of the **E** field in the proximity of the tube, thereby making this type of transition highly improbable.

Indexing the metallic and insulating nanotubes by s and m respectively, we can calculate the energies of the transitions by applying the *tight-binding model* (d is the tube diameter):

$$E_{ii}^{m} \approx i \times \frac{0.85}{d} \left[\frac{\text{eV} \times \text{nm}}{\text{nm}}\right] \tag{2.2}$$

$$E_{ii}^{s} \approx i \times \frac{2.55}{d} \left[\frac{\text{eV} \times \text{nm}}{\text{nm}}\right] \tag{2.3}$$

As it is apparent, these transition energies depend strongly on the tube diameter. However, more detailed calculations show that significant SWCNT geometry dependent deviations occur for nanotubes with diameters smaller than 1.5 nm.

When these transitions occur, the resulting excited electron and hole form a quasiparticle: a so-called *exciton*. This is a bound state of the two particles, which can be handled (mathematically) similar to a hydrogen atom. In a bulk material, these have a comparatively low ($E_{exc} \approx 25$ meV) typical binding energy, because the Coulomb-interaction between the electron and the hole is screened by other electrons. In a (quasi) one-dimensional material, however, the screening only occurs along the axis. This means that binding energies can be much higher (up to 0.4 eV). Weakly bound excitons are also present, however, the probability of generation shifts in favor of the bound ones.

When considering the different "states of the nanotubes" in this thesis, it is actually the states of the excitons we talk about. There can exist more than one excitons on a given tube, but these act as independent systems as far as we are concerned. Another interesting property to note: experiments have shown that, since nanotubes tend to "bundle" together, excitons can travel from one nanotube from another (see [8]). For this to happen, the recipient nanotube has to have lower energy excitonic levels than those of the donor's, as it is shown in Figure 2.4.

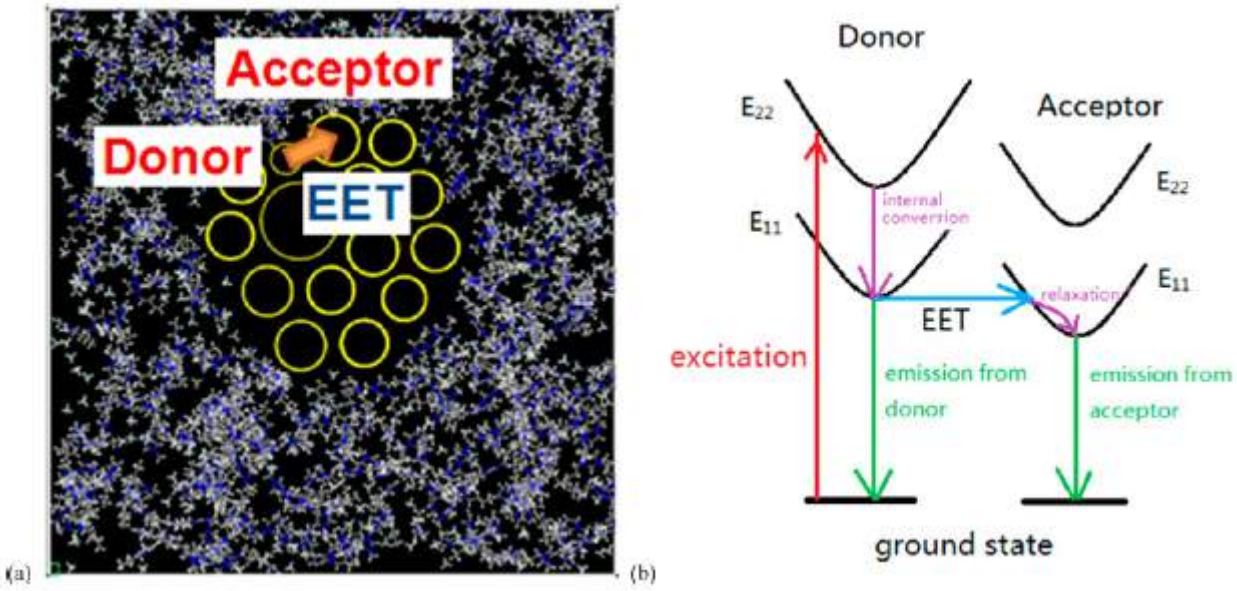

Figure 2.4: The exciton energy transfer process between bundled nanotubes. Source: [8]

2.2 Optical spectroscopy

2.2.1 Photoluminescence

Luminescence is defined as the radiation emitted by a molecule, atom, or crystal, after it went to an excited state by absorbing energy. If this energy came in the form of a photon, the process is called photoluminescence.

First, we need to consider the various possible electronic states of the excitons being investigated. In the ground state, the net spin of the exciton can only be $S = 0$ (singlet). If the quasiparticle is excited, the net spin can be $S = 1$, which corresponds to a triplet configuration (see below).

A singlet is an electronic state with a total spin of zero. In Dirac notation, this state is represented like this:

$$\Psi_S = \frac{1}{\sqrt{2}}(|\uparrow\downarrow\rangle - |\downarrow\uparrow\rangle)$$

In contrast to this, a triplet is a set of three states, each having a total spin of 1:

$$\Psi_T = |\uparrow\uparrow\rangle$$
$$\Psi_T = \frac{1}{\sqrt{2}}(|\uparrow\downarrow\rangle + |\downarrow\uparrow\rangle)$$
$$\Psi_T = |\downarrow\downarrow\rangle$$

These two types of states have very different properties, and transitions between them are forbidden in first order. Figure 2.5 shows the Jablonski diagram for a typical photoluminescent system: S_1 and S_2 are excited singlet states, while T_1 is the triplet cor-

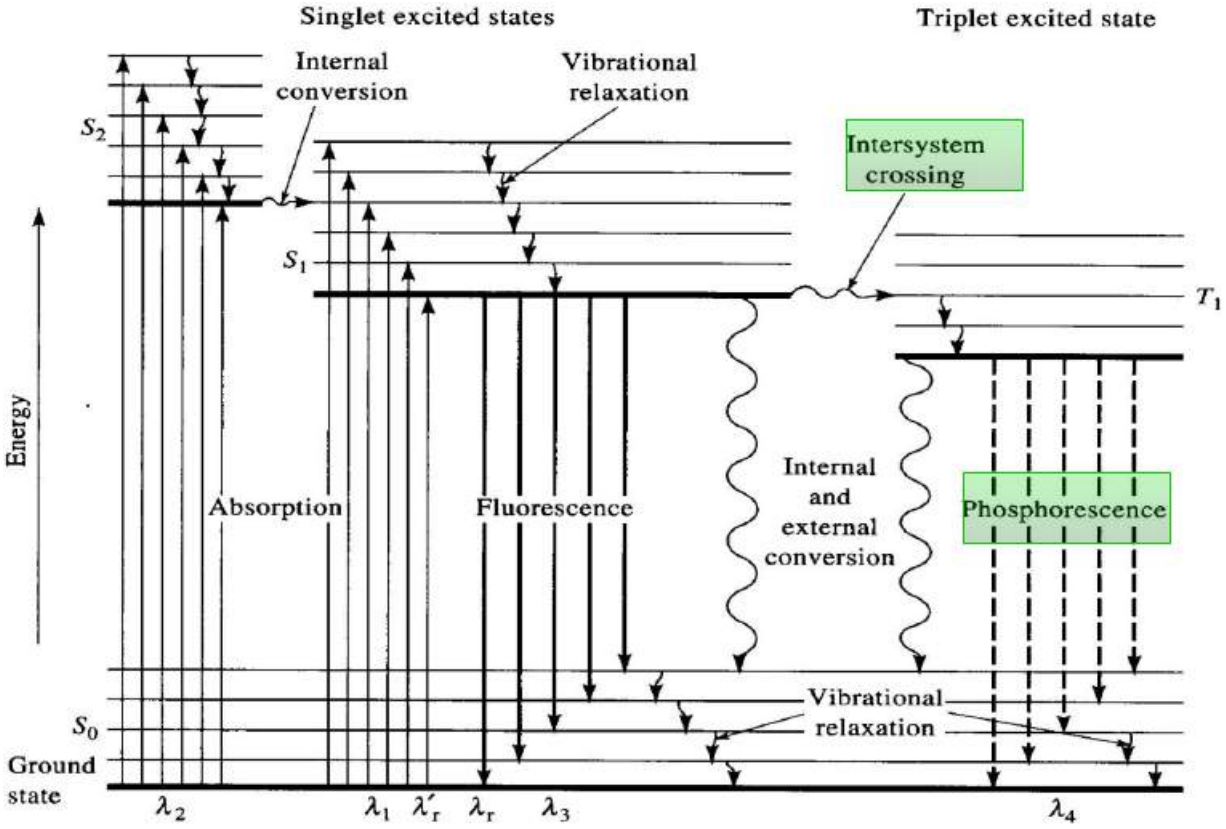

Figure 2.5: Partial energy diagram for a photoluminescent system (Jablonski diagram). Source:[9]

responding to S_1. The first thing to observe is that each state has vibrational levels superimposed on it. These levels correspond to changes in the vibrational state of the molecule, without major changes in the electron configuration. After the molecule (or in our case, nanotube) has absorbed a photon, it may radiate it back from the same vibrational level it was excited to, or it can undergo vibronic changes before reradiating. This, of course, causes the emitted photon to have a different energy compared to the absorbed one.

Which of these two possibilities is most probable depends on the environment of the molecule. When the molecule is separated (in a gas phase, for example), it has no way to get rid of the excess vibrational energy, except by emitting an infrared photon and

then returning to the ground state by emitting another photon. This, however, is less likely than the molecule returning to the ground state by emitting a single photon, that is why we observe emissions from higher excited states in such cases.

However, there are cases when the molecule can get rid of the excess energy through other process, for example transferring it to a solvent. This alternative process is usually far more efficient, so almost all emissions will happen from the lowest possible vibrational level of the excited state. This emission process is called *fluorescence*.

Often the higher vibrational states of S_1 and the lower levels of S_2 overlap. This means that there exists a coupling between these two states, giving rise to an efficient way for crossing over from one excited state to another. Taking these observations into account, one can formulate the following rule: *In a solvent, photoluminescent emission of a molecule will always happen from the lowest vibrational level of the lowest excited state, regardless of the original state the molecule was excited to.* This is known as *Kasha's rule* [10].

Taking another look at the Jablonski diagram, we note that there is no direct path from the ground state to the triplet states of the system. This is because these transfers are forbidden in first order. However, there is a path from S_1 to T_1. The process, which is called *intersystem crossing (ISC)*, is made possible by spin-orbit coupling. Theoretically, this could occur from the ground state as well, however, it is a weak process. The reason why it is more probable from the excited state is because that state has a higher impulse moment, thus participating more strongly in the spin-orbit coupling. It is important to mention that this crossing will always occur from the lowest excited state, since vibrational relaxation occurs much faster than ISC. Another important thing to note is that there is no guarantee that the three triplet levels are populated equally, nor that they have the same lifetime.

If the conversion process does happen, the system arrives at some vibrational level of the triplet state, then goes through vibrational relaxation again, before arriving at the zeroeth triplet state. Because the lifetime of such a state is generally 4-8 orders of magnitude longer than that of an excited singlet state, there is a much higher probability of losing the excitation energy by collisional transfer. At room temperature, this will be the dominant process. However, if the investigated system is held at a relatively low temperature, or collisional processes are minimized, a radiative transition from the triplet to the ground state is observed. This is called *phosphorescence*.

As the focus of this thesis is nanotubes, let us now consider how the aforementioned processes happen on their peculiar band structure, shown in the previous section (figure 2.3). We can assign the $S_0 \rightarrow S_1$ transition from the Jablonski diagram to the E_{11} excitation in the DOS, the $S_0 \rightarrow S_2$ to the E_{22} excitation and so forth. We see that, as opposed to the general Jablonski diagram shown earlier in Figure 2.5 where there were discrete vibrational levels, there is a continuum of states between each of the van Hove singularities, except the lowest ones in case of insulating nanotubes. This is also the reason why metallic carbon nanotubes do not show fluorescence as they have a continuum of states throughout.

2.2.2 Lasers

Conventionally, there is no need for lasers in photoluminescent spectroscopy. Since PL is a strong process, sufficient signal-to-noise ratios are easily achieved even with a broandband source, such as a xenon lamp, combined with a premonochromator. These

arrangements usually allow only a few mW-s at the sample.

However, in optically detected magnetic resonance spectroscopy, we need significantly higher light intensities to get discernible signals. As such, the only viable option is a tunable laser, since these are capable of providing the needed light intensities. We can group the types of lasers either by working time (continous or pulsed), or by their method of operation. They are as follows, in ascending order of their representative linewidths.

- Gas lasers
  The first type of laser to operate continously. Its lasing medium is some kind of gas mixture (Ar-Kr, He-Ne). A common property of these kinds of lasers is that they are able to operate on multiple different (but discrete) wavelengths, corresponding to the different optically allowed transitions between the electron states of the gas ions. Gas lasers are pumped by means of an arc discharge: a high voltage and an ionizing radio-frequency field maintains a discharge of the gas and the collision between the ions provide a continuous excitation..

- Solid state lasers
  The active medium of this type of laser is generally some kind of crystal, or glass doped with rare earth metals or transition metal ions. These dopants are chosen because they have a low nonradiative loss rate. This is because their excited states are weakly coupled to the phonons of the crystal lattice and are thus unable to convert the energy of the excited states into thermal energy efficiently. There are several hundred different types of these lasers. The ones widely used are Nd:YAG (neodimium doped yttrium-aluminum garnet), Nd:glass, ytterbium doped glasses, and Titanium:sapphire. Since they can be used at high power levels, they are useful in the industry and can also be frequency doubled (or tripled), giving access to previously unreachable wavelengths. Solid state lasers are usually pumped optically e.g. by a flash lamp or a pump laser. E.g. the Nd:Yag laser is usually pumped by an 810 nm diode laser.

- Semiconductor laser
  In this type of laser, light is emitted by a laser diode. Technically, semiconductor lasers are all solid state lasers but are commonly categorized on their own. The advantages of these lasers are that they can easily be integrated into electrical circuits and are small in size. The light emission occurs in a similar fashion to light emitting diodes when the current flows through a pn junction, however the special construction of the diodes allows for a coherent photon emission.

- Pumped tunable lasers
  The main characteristic of these lasers is that population inversion is achieved by another, the so-called "pumping" laser. Typically this is some high intensity solid-state laser, with an emission wavelength on or close to the absorption maximum of the laser medium of the pumped laser. One often used example is the aforementioned Nd:YAG laser, and it's frequency-doubled version. Typical examples of these lasers are free electron lasers, liquid crystal lasers, optical parametrical amplifiers, dye lasers and Ti:Sa (titanium-doped sapphire lasers). The principles and operation of the latter two will be elaborated later in detail.

Dye lasers

A dye laser uses an organic dye mixed with a solvent as a lasing medium. The dye may be placed in a standalone cuvette (not widely used) or circulated through the laser cavity. Circulation is possible in a cuvette, or in open air using a dye jet. This is needed to avoid oversaturation of the dye and also to provide cooling, otherwise the high pumping input would raise the temperature of the dye to such temperatures that it would degrade.

The dye jet is a high pressure nozzle facing a catching tube, which forms the dye flow into a sheet-like stream. The purpose of the open air design is to reduce reflection losses by eliminating the glass walls of the cuvette. As the jet operates at pressures around 4-5 bars and the dyes are usually toxic and carcinogenic, care needs to be taken that no bare skin comes into contact with the dye. As most of the dyes have absorption maxima at or around 520-530 nm, Ar-Kr lasers and frequency doubled Nd:YAG lasers are both commonly used for pumping purposes.

Ti:Sa laser

A titanium-sapphire laser is using a Ti doped sapphire crystal Al_2O_3 as its gain medium. This crystal has as exceptionally high domain of tunability, ranging between 650-1100 nm. It should be noted though, that almost none of the lasers built utilize this range fully, at least not without switching some of the optics. The reason for this is simple, currently there are no feasible solutions for making high-reflecting mirrors that can function sufficiently in the whole domain.

These lasers are ideally suited, and thus used, for ultrashort pulsed operation. This is because ultrashort pulses are used in applications where irradiation with a wide domain of frequencies is necessary. It is evident that, for example a gas laser could not be operated in this way because the range where its gain makes lasing possible, is small. In contrast to this, Ti:Sa lasers are able operate over 500 nm-s of emission wavelengths.

2.3 Optically Detected Magnetic Resonance

Optically Detected Magnetic Resonance (ODMR) is a hybrid method, combining Photoluminescent (PL) and Magnetic Resonance spectroscopy, while importing the advantageous properties of both, such as the high sensitivity of the PL and the high energy resolution of MR. The technique inherently suffers from some disadvantages as well, mainly that its use is only possible on certain molecules and crystals, i. e. those with a suitable band structure, and there are some requirements (Conditions 1-3) for the molecules optical and microwave properties, which are discussed below.

As Figure 2.6 suggests the triplet sublevels may not necessarily have the same population after the ISC process takes place (Condition 1). The reason for the population inequality is that most usually ISC is caused by spin-orbit coupling which couples differently with the 3 sublevels due to their differing spatial wavefunctions. Condition 2 is that the decay rates are also different, so that changing their population will actually change the net rate of phosphorescence. Finally, we have to be able to saturate the ESR transitions with microwave irradiation (Condition 3). If the so-called spin-lattice relaxation time, T_1, is very short, the spin populations become that of at thermal equilibrium, therefore it cannot be significantly altered by the microwave irradiation. The

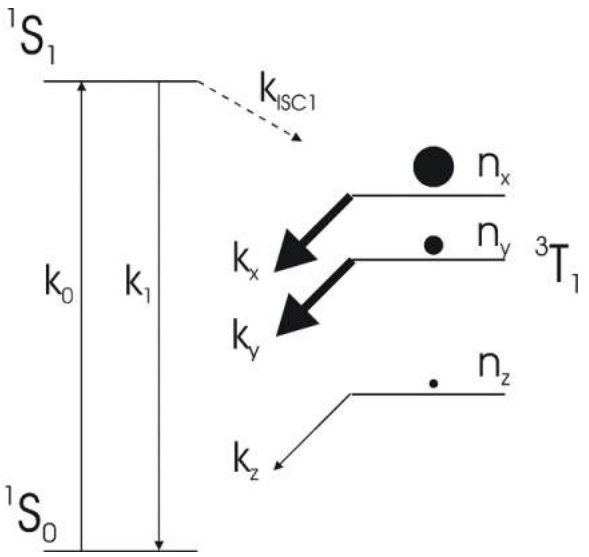

Figure 2.6: Jablonski diagram for the ODMR process for a general system. Source: [11].

precise condition is:

$$\gamma^2 B_1^2 T_1^2 \gg 1 \tag{2.4}$$

where B_1 is the strength of the magnetic component of the microwave field, $\gamma/2\pi = 28\,\mathrm{GHz/T}$ is the electron gyromagnetic ratio.

The differential equations describing the population dynamics between the five states, which are shown on Figure 2.7 are as follows (source: [11]):

$$\frac{\mathrm{d}S_0}{\mathrm{d}t} = -k_0\left[S_0\right] + k_1\left[S_1\right] + \sum_{u=1}^{3} k_u\left[T_u\right] \tag{2.5}$$

$$\frac{\mathrm{d}S_1}{\mathrm{d}t} = k_0\left[S_0\right] - k_1\left[S_1\right] - \sum_{u=1}^{3} k_{ISC} P_u\left[S_1\right] = k_0\left[S_0\right] - k_1\left[S_1\right] - kISC\left[S_0\right] - k_1\left[S_1\right] \tag{2.6}$$

$$\frac{\mathrm{d}T_u}{\mathrm{d}t} = k_{ISC} P_u\left[S_1\right] - k_u\left[T_u\right] \tag{2.7}$$

where p_u are the relative populating probabilities of the three triplet sublevels from the intersystem crossing.

We show that a continous irradiation with photons having the same energy as the gap between the sublevels will always move the system towards equilibrium. (This is the reason why a two-level system cannot function as an optically pumped laser, population inversion is impossible to maintain.)

First, we consider *Fermi's golden rule*, which gives us the transition probability per unit of time for a given system in the first order of perturbation:

$$w_{i\to f} = \frac{2\pi}{\hbar}\left|\left\langle f|\hat{K}|i\right\rangle\right|^2 \rho(E_i)\delta(E_f - E_i) \tag{2.8}$$

Where w is the transition probability, f and i designate the ending and the starting state, respectively, and $\hat{K}$ is the operator of the transition.

Applying Eq. (2.8), one can derive the transition probabilites for absorption and

stimulated emission:

$$w_{stim.em.} = \frac{1}{3}\omega_k^3 \left(\vec{d}_{fi}\right)^2 \frac{n_k}{\pi c\hbar} \tag{2.9}$$

$$w_{abs} = \frac{1}{3}\omega_k^3 \left(\vec{d}_{if}\right)^2 \frac{n_k}{\pi c\hbar} \tag{2.10}$$

Where ω_k^3 is the frequency of the incoming photon, n_k is the number of photons, and $\vec{d}$ is the transitional dipole moment ($\mathbf{d} = \sum_n \rho_n \mathbf{r_n}$).

The only difference in probability comes from the transitional dipole moment $\vec{d}$, and the equation is dependent only on its magnitude. If we consider absorption and stimulated emission between two levels, it will be clear that the probabilities will be exactly the same. Now we write the following differential equations for the populations:

$$\frac{\mathrm{d}n_1}{\mathrm{d}t} = n_{1,0} + w_{21} \cdot n_2 - w_{12} \cdot n_1 \tag{2.11}$$

$$\frac{\mathrm{d}n_2}{\mathrm{d}t} = n_{2,0} - w_{21} \cdot n_2 + w_{12} \cdot n_1 \tag{2.12}$$

The equations are symmetrical, we can see that no matter what the initial conditions, the system will always converge to equal populations. This is the fact that we take advantage of. The strength of the PL signal (red arrow on Figure 2.7) has a dependence on the population of S_0. As we have seen, if we expose the system to strong microwave radiation, and use a magnetic field to align the difference between two levels, we will change the strength of the phosphorescence peak (green path). However, the PL signal will also change, because the population of S_0 will either increase (or decrease). The greater (or lesser) population will mean more nanotubes can participate in the fluorescence cycle. This is a small change, because the weakness of the $S_1 \rightarrow T_1$ transition, three-four orders of magnitude smaller relative to the signal. This means that for ODMR to be measured, one has to achieve a signal to noise ratio of at least this difference but preferably up to 10^5. From this we know that a conventional fluorescence spectrometer has to be improved before it can be used in this manner. Also, it is absolutely necessary to use lock-in techniques, since we want to isolate a small signal from a large background.

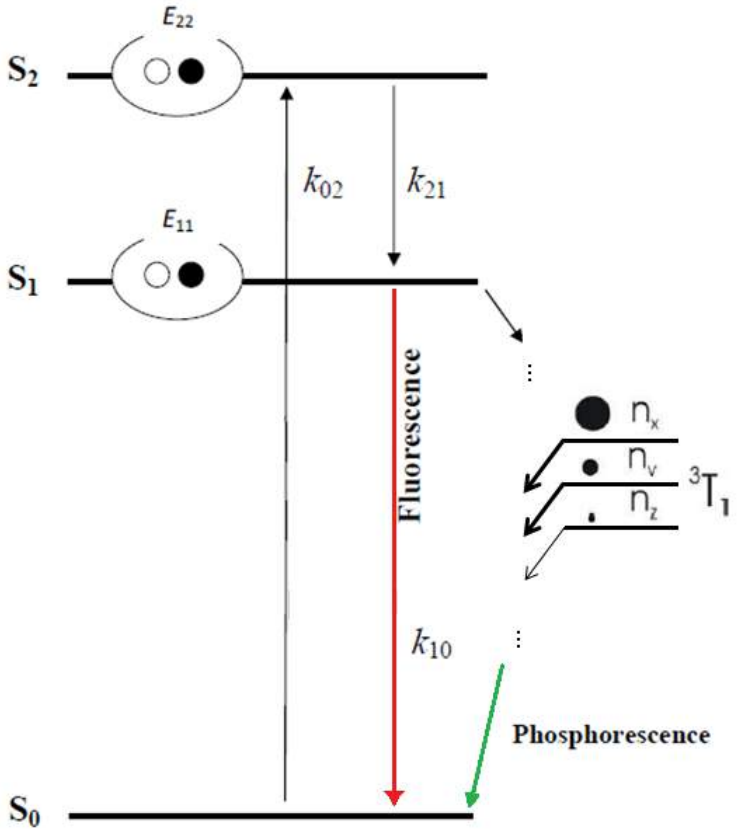

Figure 2.7: Jablonski diagram specifically for nanotubes. The thickness of the arrows is related to the decay rate of the triplet states, while the size of the circles describe their population.

Chapter 3

Experimental developments

3.1 Measurement layout

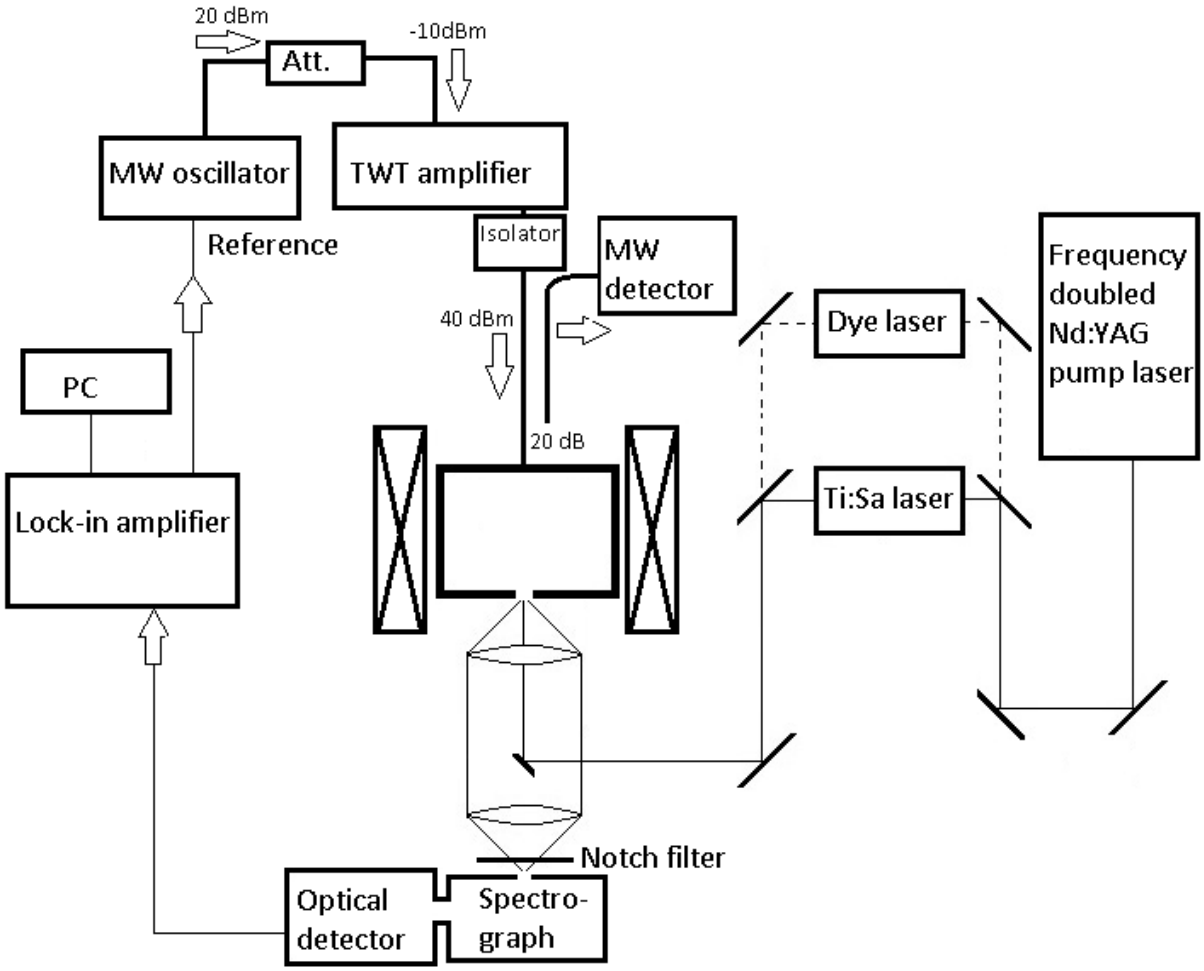

Figure 3.1: Block diagram of the measurement setup

Construction of the ODMR spectrometer presented us with a unique challenge. We needed to integrate several different measurement systems that were running on their own before, each with their own software suite. The light-gathering part of the optical

system was built on a small shelf, protruding from the optical table. This was necessary because we had to insert those parts of the optics into the magnet of the ESR spectrometer in order to be close enough to the microwave cavity to gather enough light.

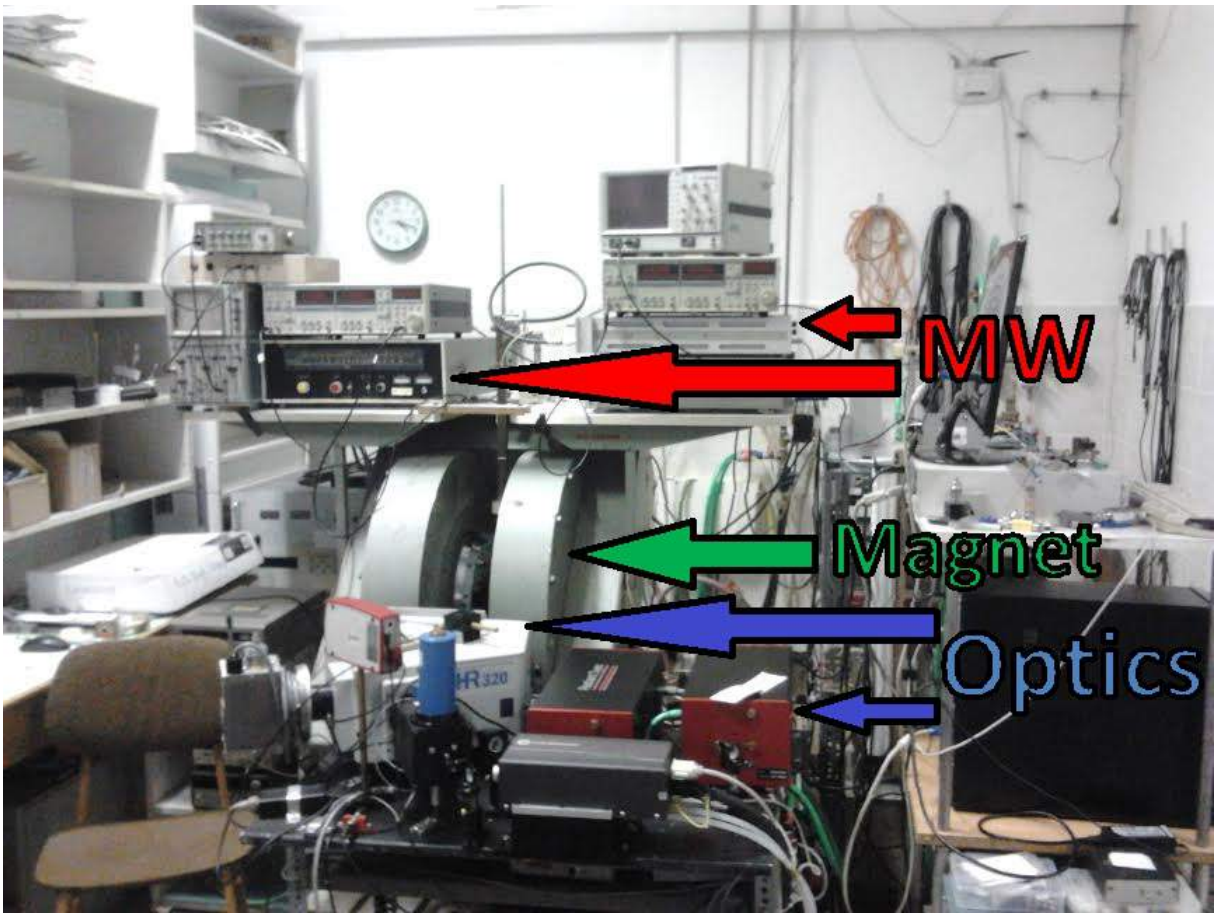

Figure 3.2: A photo of the completed measurement system.

3.1.1 The optical system

The generation of the excitation light is done by two tunable lasers, a dye laser in the lower (565-700 nm), and a Ti:Sa (700-880 nm) in the higher wavelength region. Both are from *Radiant Dyes*, and be pumped by a 5 W pump, which is an 532 nm frequency doubled Nd:YAG laser (from *Coherent*). Switching between which laser is pumped is done by replacing a single mirror.

The light leaving the operating tunable laser is guided by two mirrors to a small right-angle prism, which aligns the light path with the optical axis of the spectrometer. The light then passes through an achromatic doublet (AC254-030-B from *Thorlabs*), which focuses the light on the sample, thereby achieving greater optical power density. The same doublet acts as collection optics for the photoluminescent emissions of the sample, collimating the light beam towards the spectrometer. This is called a 180° geometry. Its main advantages are:

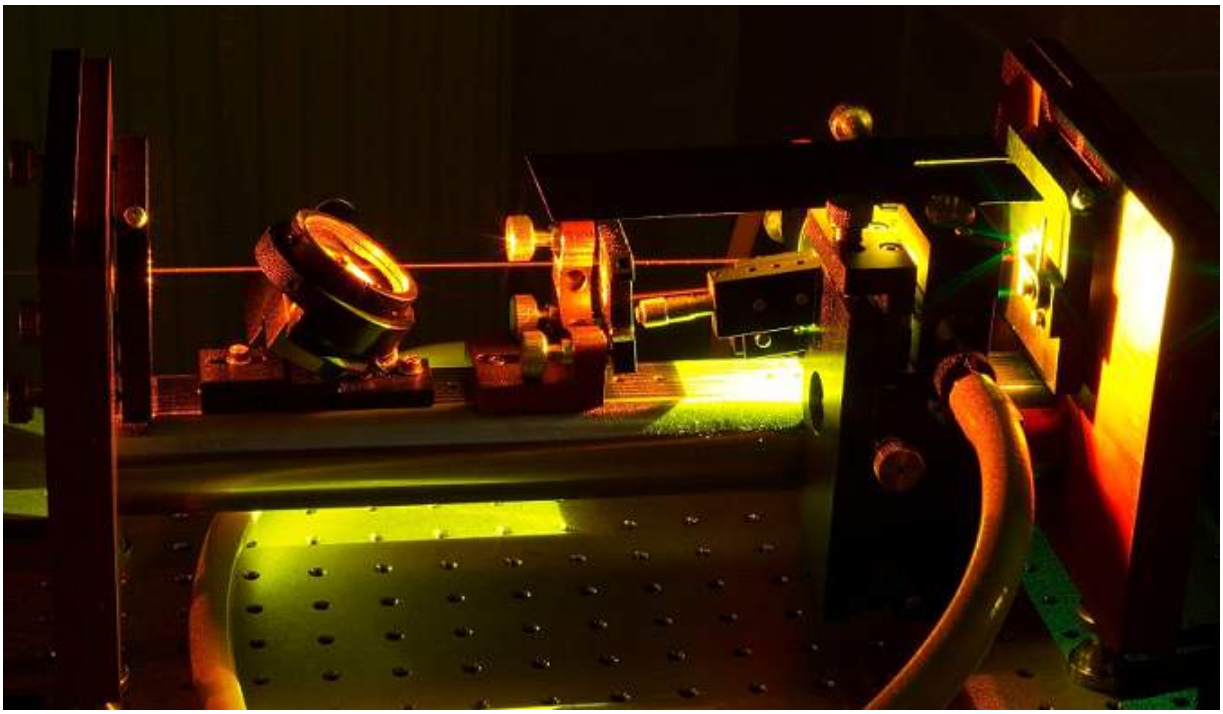

Figure 3.3: The dye laser under operating conditions. Source: [12] (Picture taken by M. Csontos.)

- This way, we inherently gather light exactly from the spot where the exciting laser is focused.
- Alignment of the light path is considerably simplified, since both the excitation and emission light has the same axis.
- Were we to employ a 90° geometry, we would need an additional opening on the microwave cavity to let in the laser light. Since any holes on the cavity decrease its performance, we wish to keep their number at the minimum.

There are some drawbacks in using this method as well: more elastically scattered light that is gathered along with the photoluminescent light than using a 90° geometry. Commercially available interferometric filters are able to fully counteract this negative effect. Also, the small right angle prism covers a small part of the collimated beam. This however, does not impact the performance of the spectrometer significantly, since there is only a loss of about 5%.

The collimated beam is focused on the entrance slit of the spectrometer by a similar lens, with an f/# matching that of the spectrometer. Before entering the spectrometer, the light encounters a long-pass interferometric filter. This serves to filter the elastically scattered light from the sample which has a wavelength similar to that of the excitation and is commonly referred to as "Rayleigh light". In an ideal case, this light component would be filtered out by the spectrograph itself, which is a movable grating monochromator. However, there are always imperfections present, e.g. diffuse scattering on the mirrors and gratings, which causes this intensive radiation to reach the detector even when it should be filtered our by the monochromator. In addition, the diffraction grating deflects light with a given wavelength along its first order and half the wavelength along

its second order. This, together with the high intensity of the Rayleigh light explains why its filtering is neccessary. We note that usual commercial spectrometers employ filters with inferior optical density thus such disturbing effects are common therein.

The spectrometer itself is a conventional (*iHR320, from Horiba JY*) Czerny-Turner configuration spectrometer with a rotating holographic diffraction grating. Its linear dispersion is defined by the following equation:

$$\frac{d\lambda}{dx} = \frac{\cos\beta}{knL_b} \tag{3.1}$$

Where λ is the wavelength of the incidental light projected onto the exit slit of the spectrometer, β is the angle of the projection, k is the order of diffraction, L_b is the distance between the grating and the exit slit, and n is the number of the grooves per millimeter on the grating.

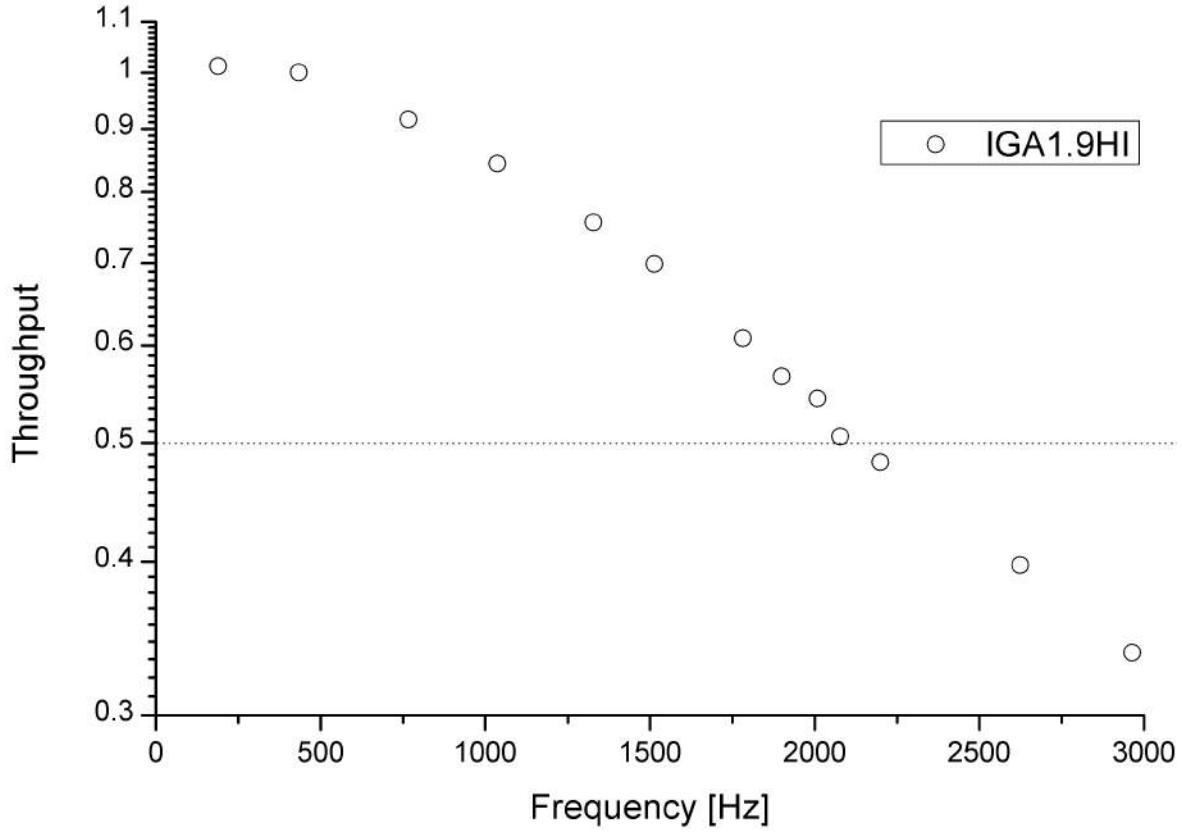

Figure 3.4: The frequency-dependent throughput of the detector. Measurement was done by selecting a PL peak, and measuring the frequency-dependent signal (with a lock-in amplifier) relative to the DC level, while the laser output was optically chopped.

The detector The spectrometer is equipped with an InGaAs detector (*DSS-IGA1.9010L*, from JY), which is suited for measuring the near-infrared emissions of the nanotubes, with a *Noise Equivalent Power* (*NEP*) of $3 \cdot 10^{-14} \frac{\mathrm{W}}{\sqrt{\mathrm{Hz}}}$. The detector has a 10× voltage amplifier, which can be turned on and off. With the amplifier on, it has a bandwidth of approximately 500 Hz, with the amplification off, a bandwidth of 2000 Hz (this bandwidth is defined by the -6dB point). These bandwidths limit the chopping frequency of

the microwaves, since we demodulate the signal of this detector with the chopping of the microwave sweeper. Thus, if the optical detector cannot admit these frequencies, one observes nothing of the ODMR signal. The preamplifier and IV converter of the InGaAs detector requires ±15 V supply voltage. As seen in Figure 3.4, soon after 1 kHz the detector begins to cut down in throughput, which means that this is the optimal frequency for the measurement, since after this, the S/N ration would begin to diminish. Since the stability of the original power supply was not sufficient for the noise levels required, we built a rechargeable battery based ultra-stable power supply, which decreased the noise level significantly.

3.1.2 The microwave system

Generation of the microwave signal was done by a *HP83751B* oscillator. This has a power-independent noise on its output, so we get the best signal-to-noise ratio for the microwaves when operating it on its highest output level (20 dBm). This output is then fed into a *Traveling-wave tube amplifier* (*TWTA*). The operation of the *TWTA* is explained in the following.

An electron beam generated by an electron gun passes through the middle of a helical RF circuit. The input to be amplified is coupled to the circuit. The EM field generated by the current in the helix causes the electrons to be velocity-modulated, forming so-called "bunches". These bunches, in turn, amplify the current with their own EM field. At the end of the helix, the amplified RF output is coupled out. The helix also acts as a *delay line* that matches the velocity of the wave (relative to the axis) to that of the electrons. This is necessary for the amplification effect to exist.

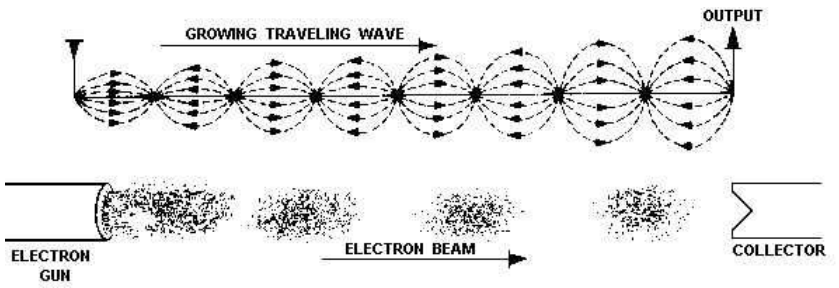

Figure 3.5: The principle of operation of the *TWTA*. Source: [13]

However, although the *TWTA* has a 50 dB amplification, its maximum output level is 40 dBm (10 W). So, the best signal-to-noise ratio is achieved by attenuating the signal coming from the sweeper by 30 dB with passive attenuators, since this lowers magnitude of both the noise and the signal equally and we still get the maximum achievable power from the amplifier. Since we use such high power levels and the sample is only a fraction of a milliliter, care needs to be taken not to melt the frozen sample with the microwave irradiation.

Connecting the output of the TWTA to the microwave cavity, is a directional coupler waveguide. It transmits the power to the cavity, while coupling a small amount of the reflected power (1:20 dB, about 1%) to the third port of the device, where a microwave detector (*HP8742B*) measures it. The coupler has a directivity of 36 dB, that is, only 0.025% of the power coming from the *TWTA* will cross over to the third port.

The microwave cavity The cavity is analogous to an RLC circuit in standard electronics. As such, the differential equation describing its behavior is as follows:

$$U = L\left(\frac{dI}{dt}\right) + RI + \frac{q}{C} \tag{3.2}$$

The impedance of the system:

$$Z = \sqrt{R^2 + \left(\omega L - \frac{1}{\omega C}\right)^2} \tag{3.3}$$

As we can see, we get the maximum current by driving the circuit on the resonance frequency: $\omega_0 = \frac{1}{\sqrt{LC}}$. We define the quality factor of the cavity:

$$Q = \frac{\omega_0 L}{R} = \frac{1}{R\omega_0 C} \tag{3.4}$$

This factor shows the ratio of the energy stored in the system, compared to dissipated in a period. Q can also be expressed by in terms of the resonance function: $Q = \frac{f_r}{\Delta f}$, where f_r is the resonance frequency, and Δf is the half-width of the resonance peak. Since the resonance of the cavity gives us a frequency to use, we cannot match the energy of the photons to the gap between two triplet levels. Instead, we use a strong magnetic field to modify the difference between the levels, and hold the frequency of the microwaves on the cavity resonance frequency the whole time of the measurement.

Automatic frequency control The strength of the ODMR signal depends on the microwave power introduced into the cavity. The cavity has to be critically coupled i.e. no power is reflected back towards the source. The signal is at maximum, if it is irradiated at the resonance frequency. However, the resonance frequency is not constant. This occurs partly because of thermal expansion, from the microwave energy which is fed to the cavity, but mostly from the bubbling nitrogen which changes the resonant frequency of the cavity.

To treat this problem, we employ a technique called *Automatic frequency control (AFC)*. First, let's take a look at the intensity (R) of the microwave EM field inside the cavity:

$$R(f) = \frac{w}{\pi} \cdot \frac{1}{(f - f_r)^2 + w^2} \tag{3.5}$$

$$\left.\frac{dR}{df}\right|_{f=f_r} = 0 \tag{3.6}$$

where f_r is the resonance frequency. The microwave power detector has an output voltage which is proportional to $R(f)$. Let us now frequency modulate our MW signal with a small amplitude:

$$f(t) = f_0 + A_{mod}\cos(\omega_m t) \tag{3.7}$$

where ω_m is the modulating frequency. This is usually in the order of 1-100 kHz.

The series expansion of the modulated signal reads as:

$$R(f) = R(f_0) + \left.\frac{dR}{df}\right|_{f=f_r} A_{mod}\cos(\omega_m t) + ... \tag{3.8}$$

Clearly, the component which oscillates with the frequency $omega_m$ is proportional to the derivative, and with the proper sign. This can be used as a feedback signal, to regulate the frequency of the source to always match the actual resonance frequency.

We have one additional factor to consider. Since for the ODMR measurement it is necessary to chop the MW signal around 1 kHz (see next section), the modulating frequency of the AFC needs to be sufficiently greater than this, so the chopping does not interfere with the frequency modulation.

3.1.3 Electronic instrumentation, software

Almost all of the instruments used in the experiment employed GPIB protocol to communicate with the controlling PC. The only exception was the Spectraq2 unit (see below), which had its own control language. However, we managed to integrate it into the main measurement program which is written is Visual Basic, by utilizing the dll files provided by the manufacturer.

Lock-in amplifier As mentioned before, the use of a lock-in amplifier (LI) is required to detect the signal with the desired S/N. This is because one has to be able to isolate a small change caused by the microwave excitation from a large photoluminescent signal. It is logical to modulate the microwaves at a certain frequency, and then measure at that given frequency with the frequency selective amplifier. To achieve this, the microwave signal generator is "slaved" to the LI, i. e. the internal reference frequency set on the LI is the one that amplitude modulates the generator.

Spectraq2 This combined power supply/detector interface unit was provided by *Horiba JY*. We used it to measure the DC photoluminescent signals on the detector during the measurements, so the ODMR and PL spectra were acquired at the exact same instants of time (less than 0.1 s difference).

The electromagnet The electromagnet of the ODMR spectrometer is composed of two coils in Helmholtz-configuration, which provide a uniform magnetic field. We are able to control the magnetic field to a degree of precision up to 1-2 Gauss. We will see later, that the width of the resonance peaks of the nanotubes are 30-40 Gauss broad, so this precision should be more than sufficient for our goals.

The program code

The documentation of the program and the code itself is be found in Appendix B. Here, we present a small overview of its functions and capabilites. The program is specified for the following tasks:

- initializing all instruments to begin measurements properly
- setting up all parameters prior to the beginning of the measurement
- taking magnetic field-swept spectra
- taking optical spectra
- taking time-resolved measurements (for later use)

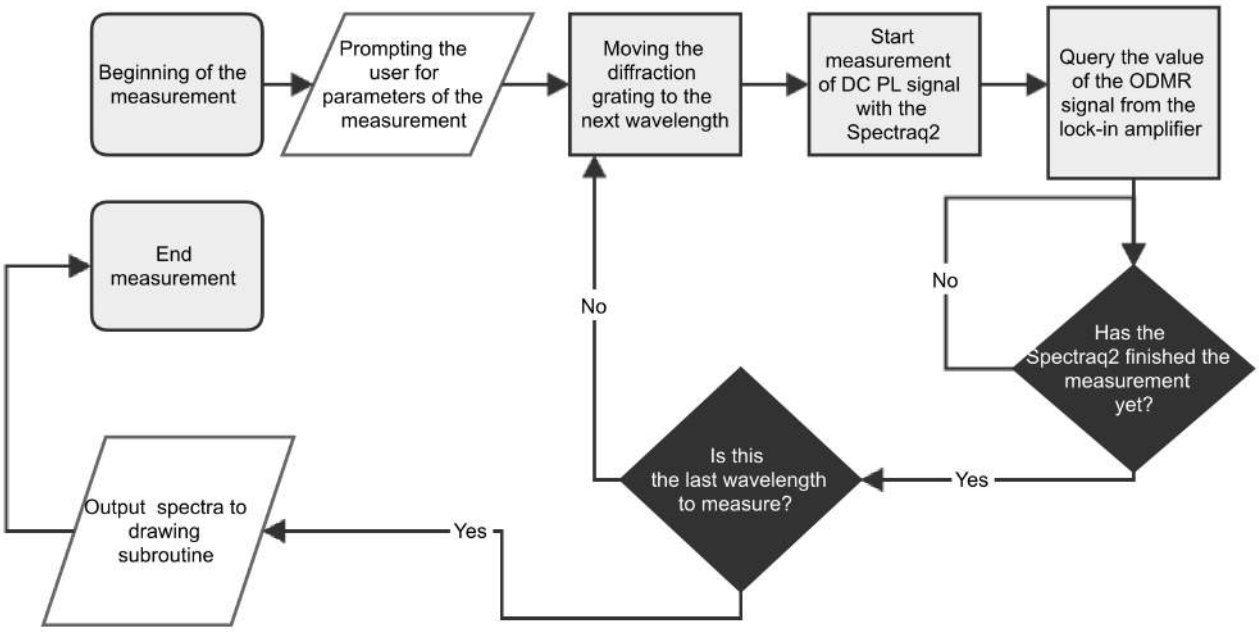

Figure 3.6: A simplified flowchart of the measurement of optical spectra by our program.

3.1.4 The samples

The samples used in the measurements are prepared in the following way: we introduced the nanotubes to distilled water mixed with DOC (sodium-deoxicholate) surfactant, and then sonicated them with a tip-sonicator device for an hour. The surfactant then bounds to the nanotubes made individual (or into smaller bundles) by the sonication, thereby preventing them from bundling again. This is neccessary as larger bundles are inactive in PL measurement. If a semiconducting tube has a metallic neighbor in a bundle, its PL is "quenched" by the metallic neighbor due to its continuum of electronic states. (Smaller bundles however, display some very interesting characteristics, which will be later explained in detail.) After the sonication, the samples are ultracentrifugated a 200 000 g for an hour. This removes the larger bundles that were not broken up by the sonication. The remaining suspension was then placed into a 4 mm diameter quartz tube, which was sealed to prevent the sample from evaporating.

To provide the sample with the necessary cooling to reach 77 K, we place the prepared sample contained in a tube into a double-walled quartz static cryostat.
This presents a distinct set of additional problems:

- Water will condense on the outer surface of the cryostat, part of which is inside the microwave cavity. Since liquid water absorbs microwaves, this will make measurements impossible. The solution for this is to circulate nitrogen gas through the cavity. The nitrogen gas coming from a tank is completely dry, thus it prevents the condensation.

- Because the nitrogen in the cryostat comes into contact with the air in the laboratory, it continously absorbs more and more water in ice form. This does not

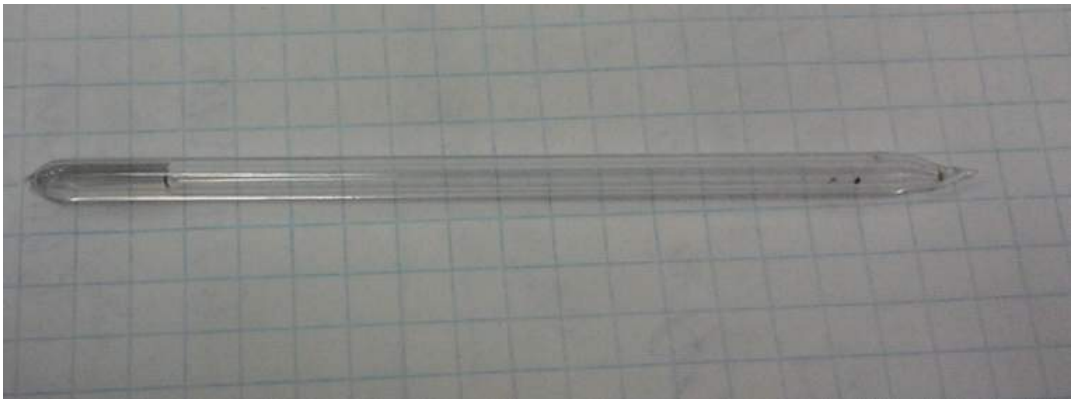

Figure 3.7: A photo of the prepared sample in the quartz tube

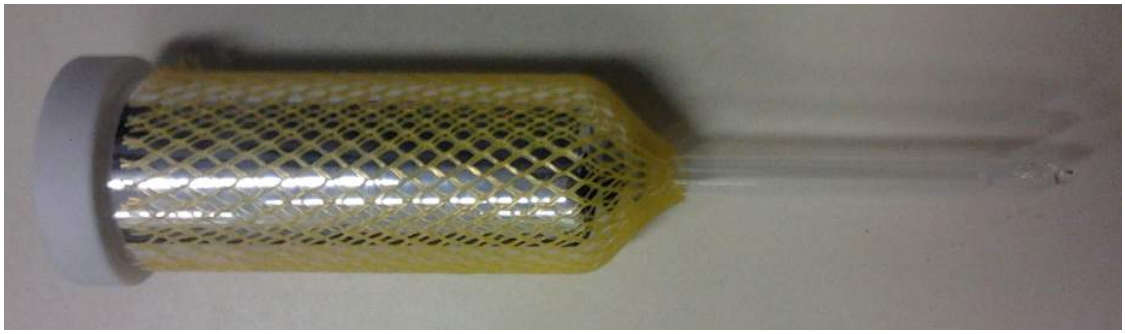

Figure 3.8: The cryostat

interfere with the MW measurement (since ice does not absorb microwaves), but the "flurry" of the ice in the lower part of the cryostat will introduce an additional noise component in the optical measurements. We solved this problem by manufacturing a cover for the cryostat, that has only a small hole in it. This way, the evaporating nitrogen creates a surplus of pressure under the cover and no air from the laboratory enters the cryostat. Some ice will still remain from the initial and subsequent fillings of the cryostat, but this is a minor quantity, and the bubbling of the boiling nitrogen keeps them from the optical path. The cover was made from teflon, which has a thermal expansion coefficient similar to glass, preventing it from cracking the top of the cryostat as a metal cover would, when cooling down.

- The aforementioned boiling forms bubbles traveling upward from the bottom of the cryostat, often crossing the path of the exciting light. This introduces a large noise into the measurement (compared to the 10^5 S/N ratio we need to achieve). The solution for this problem is explained in detail in a later chapter.

- Since the nitrogen needs to be refilled multiple times during a measurement, it is a challenge to prevent the cryostat (and with it the sample) from changing position inside the cavity and at the same time, allow it to be rotated during the initial setup. A satisfactory solution to this problem is yet to be found itself.

3.2 Noise reduction

Here, we describe the factors that contribute to the noise and what was done to decrease each of them. At first, when measuring PL at 77 K, we encountered S/N ratios ranging in the 10^3-s, when measuring the noise at 1.2 kHz. As mentioned above, the expected ODMR/PL ratio is about $10^4 - 10^5$, therefore, this noise level meant an undetectably low value for the observation of PL. As a result a 100 fold increase of S/N had to be achieved. The main sources of noise were (listed in order of contribution to the noise level):

- the intensity noise of the laser (*Relative Intensity Noise, RIN*)
- the bubbling of the nitrogen, which affects the light path and also the resonance frequency of the microwave cavity.
- the noise arising from the mechanical vibrations originating in various components
- the noise due to the shifting of the resonant frequency of the cavity

3.2.1 Laser intensity noise

The intensity noise from the laser can also be attributed to several factors (again listed from largest to smallest):

- Improper alignment of the laser. While it is capable of operating with the required intensity output (300 mW at the sample) at a fairly wide range of alignment parameters, low-noise operation takes a considerable effort to achieve. Detailed instructions on the method of properly aligning both of the lasers in the experiment, can be found in Appendix A. The noise of the laser when not properly aligned is a low background with sporadic Dirac-delta-like components, making measurements impossible.
- Dust buildup. The laser needs to be cleaned daily, to be able to operate with the required parameters. Isopropylene suffices for this because there are no actual stains on the surfaces to remove.
- The noise of the pump laser. When removing the aforementioned factors, this is the only one that remains (besides the inherent stochastic noise of the pumping). If only this remains, the relative intensity noise (RIN, defined below) of the laser equals or is below -54 dBc@1.2 kHz.

The RIN of the laser was measured by an optical power meter (*Thorlabs PM100D*) with a photodiode sensor (S130C) that was capable of high-bandwidth measurements (up to 100 kHz). This was coupled to a lock-in amplifier, with an internal reference frequency set to the values shown on the diagram. Noise was measured with the built in noise measurement function of the lock-in and the noise voltage was converted back into intensity. Figure 3.9 shows the measured relative intensity noise (in dBc units) of the laser output as a function of the offset frequency from the carrier. The dBc units refer to the relative power with respect to the carrier, i.e. $\mathrm{RIN} = \log_{10}\left(\frac{\delta P}{P_\mathrm{c}}\right)$, where P_c is the DC power of the laser, δP is the noise of the power.

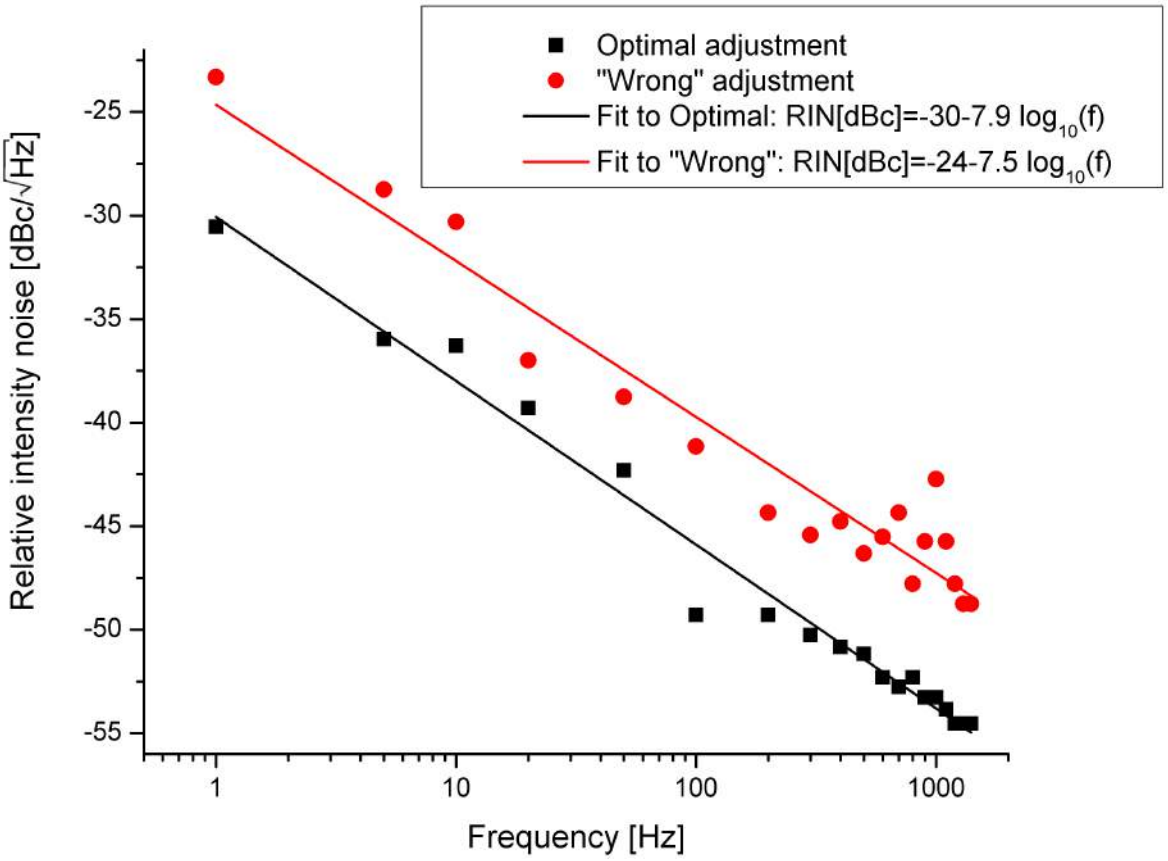

Figure 3.9: The relative intensity noise of the laser as a function of the frequency on a double logarithmic plot.

We fitted the RIN versus f phenomenologically with a logarithmic function for two adjustments, optimal and "wrong", with parameters shown in the Figure. Remarkably, the RIN slope for the two adjustments appears to be similar and it is the vertical offset value which is different, the "wrong" adjustment being some 6 dBc higher. Since the detector voltage (and the ODMR signal) is directly proportional to the power and its noise, it means that this "wrong" adjustment would give rise to a factor 4 worse signal to noise ratio. It is a common knowledge in laser science [14] that RIN is larger if the laser does not operate at high gain as therein, the spontaneous emission (which is inherently random) can have a large effect on random power fluctuations. This explains why the above two factors, improper laser alignment and dust build-up, contributes to higher laser noise. We also found that lower pump laser energies are also not optimal for the laser noise and it is better to operate the pump laser with maximum power and to attenuate the tunable laser output power outside of the laser.

We note that the RIN=-54 $\frac{\text{dBc}}{\sqrt{\text{Hz}}}$ around 1 kHz means a signal to noise ratio in the detected power of 2×10^5. As we mentioned above, we targeted this value as an ideal goal for the overall spectrometer setting. This is due to the fact, that the ratio of a typical PL peak (4 V) and its noise (20 μV) is exactly 2×10^5. Therefore the choice of a lock-in frequency near 1 kHz is optimal in our case, in our case, given that for higher frequencies the detector response starts to decrease as we discussed it above.

3.2.2 "Bubble noise"

The next factor in order of contribution was the noise generated by the bubbles of the boiling nitrogen crossing the light path. This had a considerable component even at our measurement frequency. A smaller, but still significant effect is that the bubbles move the sample around, if it is not properly affixed.

First, we tried to hold the sample in place with a rigid fixture. This eliminated the movement of the sample. However, we did not succeed in blocking the bubbles from the light path by positioning the sample close to the wall of the cryostat, because the fixture would break too easily. It became evident that we need an elastic fixture, and the sample needs to be affixed to the wall of the cryostat locally.

The next solution was to employ a fixture with a joint, combined with fixing the sample with vacuum grease to the walls. When subjected to 77 K, the grease becomes somewhat opalescent but no significant decrease to the signals was measured. This kept the sample immobile and the bubbles could only emerge on the other side of the cryostat. This method succeeded partially, as we could make measurements without the noise interfering. All the measurements later in this thesis were done by employing this method. However, this solution still suffers from some drawbacks. First, the placement of the sample inside the cryostat is not robust, each time when a replacement is made, several tries are necessary to correctly place the new sample. Also, the ice contamination mentioned before gets a lot worse while using this method, as the grease is hidrophylic, and brings a lot of ice to the cryostat. This results in having to adjust the sample quite often, which is troublesome during a measurement.

Most recently, our solution has been to wedge the sample at the end of the cryostat with a small piece of teflon tape. As teflon has a similiar thermal expansion coefficient than that of quartz, there is no danger of cracking the cryostat. So far, this method has not developed any kind of drawbacks, however, it remains to be fully tested.

The presence of bubbles also affect the resonant frequency of the cavity. The liquid and gaseous nitrogen have different density, therefore, when a bubble moves from the bottom of the cryostat, the net amount of nitrogen dielectric changes inside the cavity, which results in a random and uncontrolled microwave resonant frequency.

This can be tackled by using an AFC circuit (as it was discussed above). The parameters of the AFC are optimized for a rapid feedback. In particular, the time constant of the feedback time is shorter (10 ms) than it is usual in ESR spectroscopy (30-100 ms). This as we found was sufficient to keep the microwave source locked to the resonance of the cavity for the duration of the measurement.

3.2.3 Vibrational noise

Vibrational noise originates in several of the equipment used in the measurement. Examples of this include:

- the cooling fan of the chiller of the pump laser
- the pump of the dye laser
- cooling of the MW sweeper, LI amplifier, TWTA
- general vibrations from the laboratory

Most of these problems were eliminated by building a movable optical table through fastening an optical breadboard to a rolling cart. This in turn, can be fixed to the ESR spectrometer, weighing over 2 tons. Without the optical table, vibrations would disrupt the measurements too much, because there is no way to put some of the noise-generating equipment further apart from the experiment.

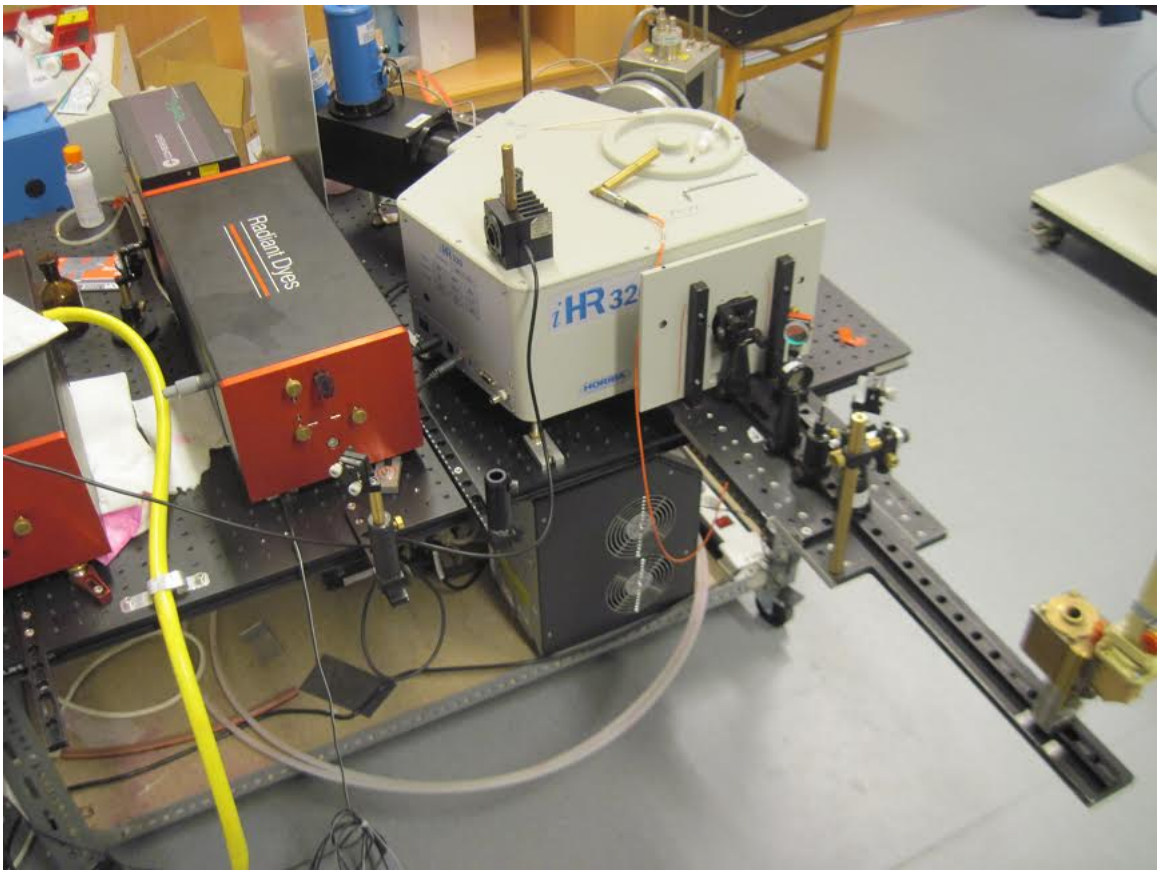

Figure 3.10: A photo of the movable optical table, with the lasers and the spectrometer on it

3.2.4 Final considerations

A common knowledge in spectroscopy is that noise of a well designed system is given by that of the detector. Usually, detectors operate close to some physical or technical limitations, therefore, their noise cannot be reduced any further. This also means that noise contributions from other external sources are reduced below the level that they could contribute significantly to the net noise. When we have a 4 V PL line, the noise of the system is around 40 μV (this and the following in this paragraph were measured at 1.2 kHz). This corresponds to a S/N ratio of 10^5. However, the detector's dark noise is only 20 μV. The rest is the shot noise of the measurement (since these two noises are independent, they add up squarely, so the real value of the shot noise in itself is: $\sqrt{40^2 - 20^2} \approx 35\mu$V). This means that apart from gathering more light or making the sample more concentrated to increase the light output, we have no means of further increasing the S/N ratio. In any case, the detector can measure only up to 10 V, so we

would only gain a factor of $\sqrt{2.5}$ of this. This is because when the shot noise dominates the measurement, as it is in this case, the S/N only increases with the square root of an increase in the signal. The reason for this is in statistics: photoluminescence can be described by a Poisson process, which has a standard deviation that equals the square root of the mean value (in our case, the measured signal). A demonstration of this effect can be seen in Figure 3.11.

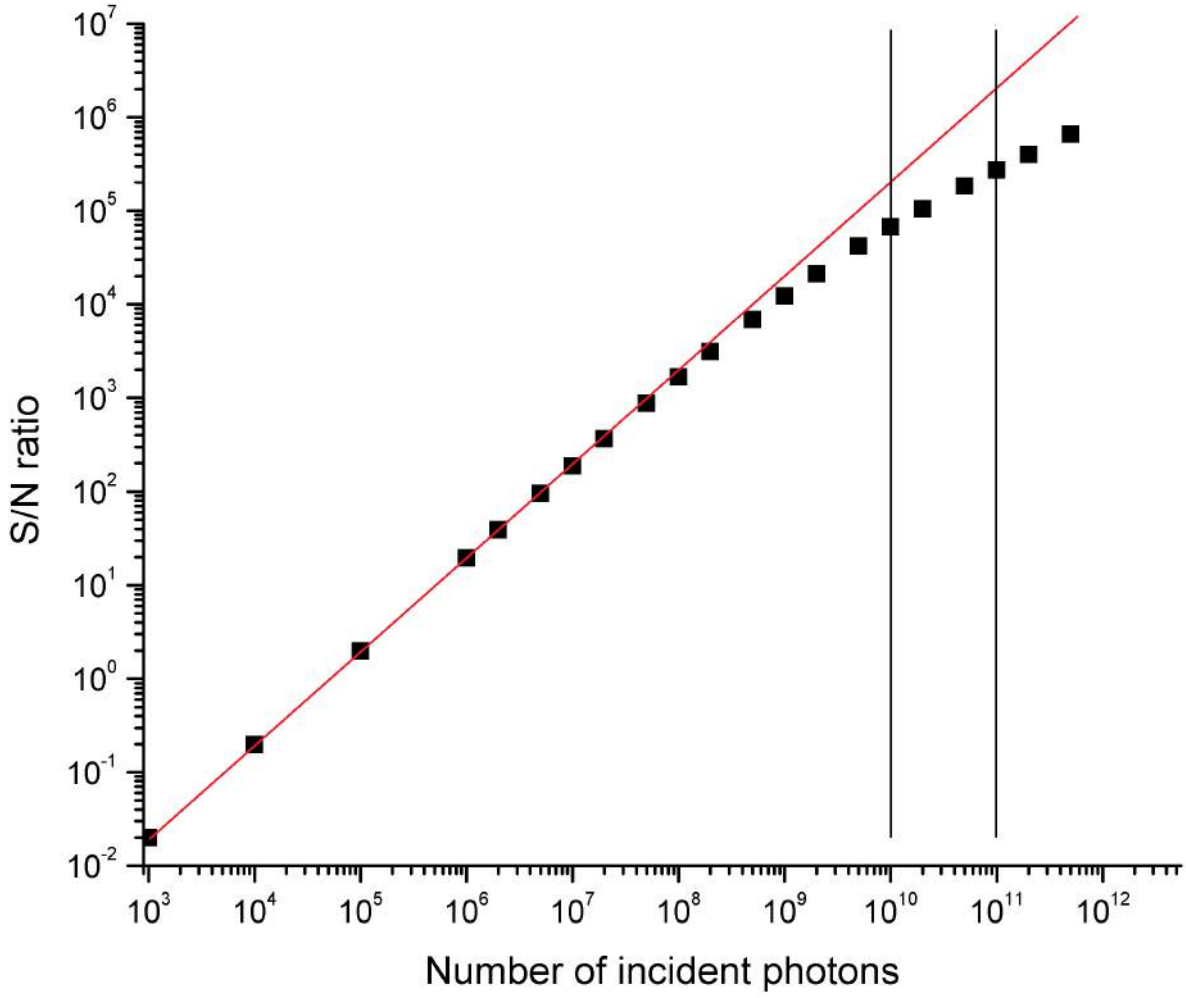

Figure 3.11: A demonstration of the increase of the S/N ratio with the increase of the incident photon number. Black lines show the region of our measurements.

The data used to create Figure 3.11 comes from the following considerations:

1. We assumed all photons have an energy corresponding to a wavelength of 1000 nm (2×10^{-19}J).
2. The detector has a responsivity of $2 \times 10^9 \frac{\mathrm{V}}{\mathrm{W}}$ at this wavelength.
3. From 1. and 2. we get the following conversion factor: $U = C \times n$, where $C = 4 \times 10^{-10}$V, n is the number of the photons detected.
4. The detector has a noise of 20 μV at 1.2 kHz.

5. Since the noise of the detector and the shot noise of the photoluminescence process are independent, they have to be summed squarely.

6. Employing the above, we can calculate the net noise on the detector originating from the inherent and the shot noise.

We tabulated the noise for a few select values and displayed them on Figure 3.11. The point where the shot noise starts to overtake the detector noise is when the standard deviation of the Poisson process converted to detector voltage begins to exceed the 20 μV constant noise of the detector. This happens at a standard deviation level of 50000 photons, which amounts to a mean of 2.5×10^9 photons in the Poisson process. That in turn will generate a signal of 1 V mean value on the detector output.

The only method for raising the S/N ratio significantly would be a detector with a higher detection limit, and making a more concentrated sample. This was not feasible for us for the time being.

Chapter 4

Results and discussion

The fact that there was no known case of ODMR being measured on a nanotube sample meant that we faced some difficulty with our first measurements. We had to assume that the ODMR peaks of the tubes were at the same wavelength as the PL peaks. As show later, this assumption holds although there is a small shift between the PL and ODMR peaks. In addition, nothing was known about the spin-relaxation properties of the material at 77 K and the strength of the ODMR signal. These could have prevented the observation of ODMR. However, we succeeded in observing ODMR when setting the optical spectrometer to measure emission at the different nanotube peaks.

We briefly discuss the ODMR measurements in historical order as they were performed, then we discuss the physics at work, which follows the actual timeline less rigorously. We must keep in mind that our ODMR setup is essentially 3 dimensional, the parameters being the magnetic field, exciting and emission wavelengths. The ODMR intensity is expected to only occur when we are in resonance with all three parameters.

With the above described assumption that ODMR intensity is strongest where the PL intensity is strongest, we set our laser and spectrometer to a maximum and performed a magnetic field sweep. We did observe an ODMR signal as shown in Figure 4.1.

After the first successful observation, we verified that the magnetic resonance is the same for all nanotube chiralities and then we proceeded to perform an ODMR map measurement by means of changing the exciting laser energy and analyzing the emitted light.

4.1 Field swept spectrum

With our final goal being to take measurements on an inhomogeneous sample of an ensemble of nanotubes, first we had to determine whether every nanotube has the same magnetic resonance. We selected the tubes with the strongest PL signals, and took a magnetic field sweep while measuring with the optical spectrometer at their strongest emission frequency. Results are shown in Figure 4.1.

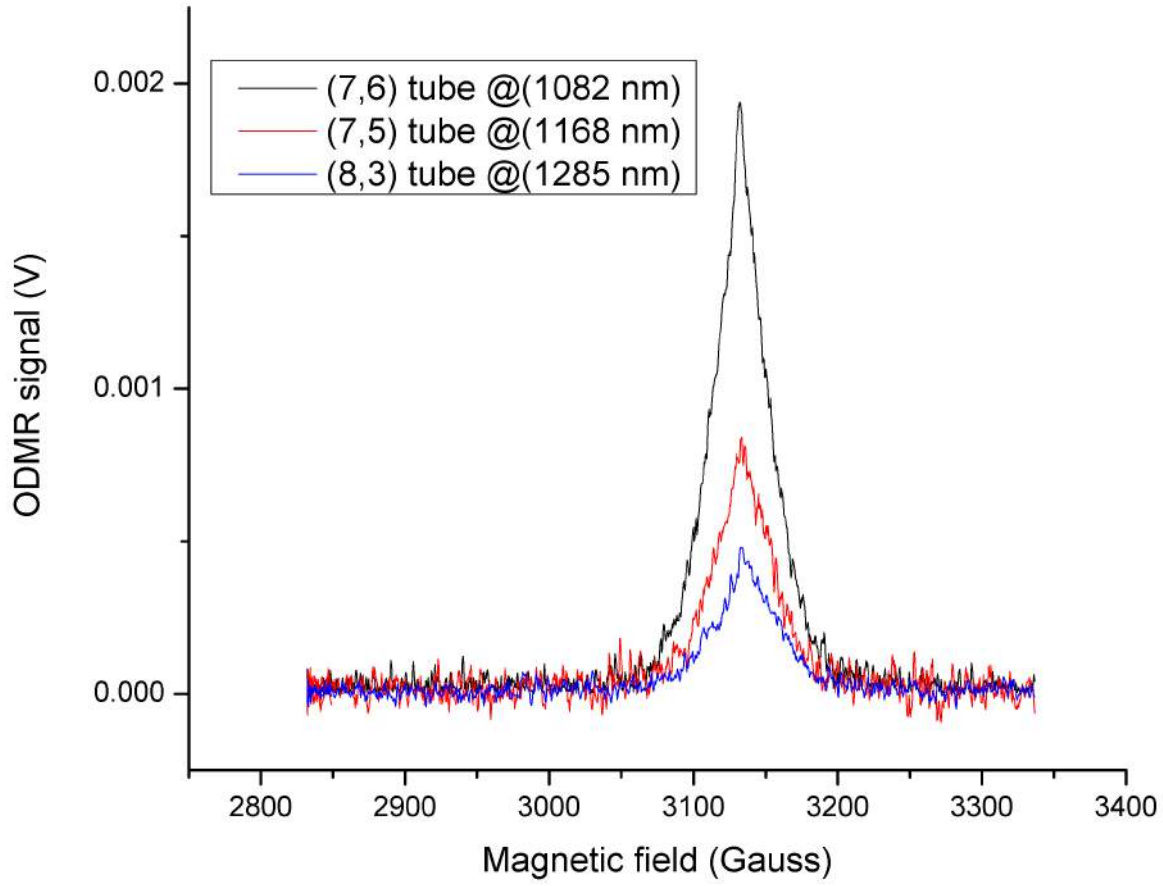

Figure 4.1: Comparing the ODMR signals of three nanotubes with different chirality, as a function of the magnetic field.

The figure demonstrates that at least for the chiralities we observe, the g-factors are the same, thus it is possible to measure their signals in a spectrum together. The magnetic field spectra have S/N ratios ranging between 20-100, this is what we also expect from the optical spectra.

4.2 Individual ODMR spectrum

After verifying that the g-factor of the tripet states is identical for all nanotube chiralities, we set the magnetic field to the resonance peak (3140 G) and proceed to perform a wavelength analysis. Results are shown in Figure 4.2.
The first interesting thing to note, that the ratio of the peaks to one another in the different spectra is not the same. This is explained by the fact that the strength of the

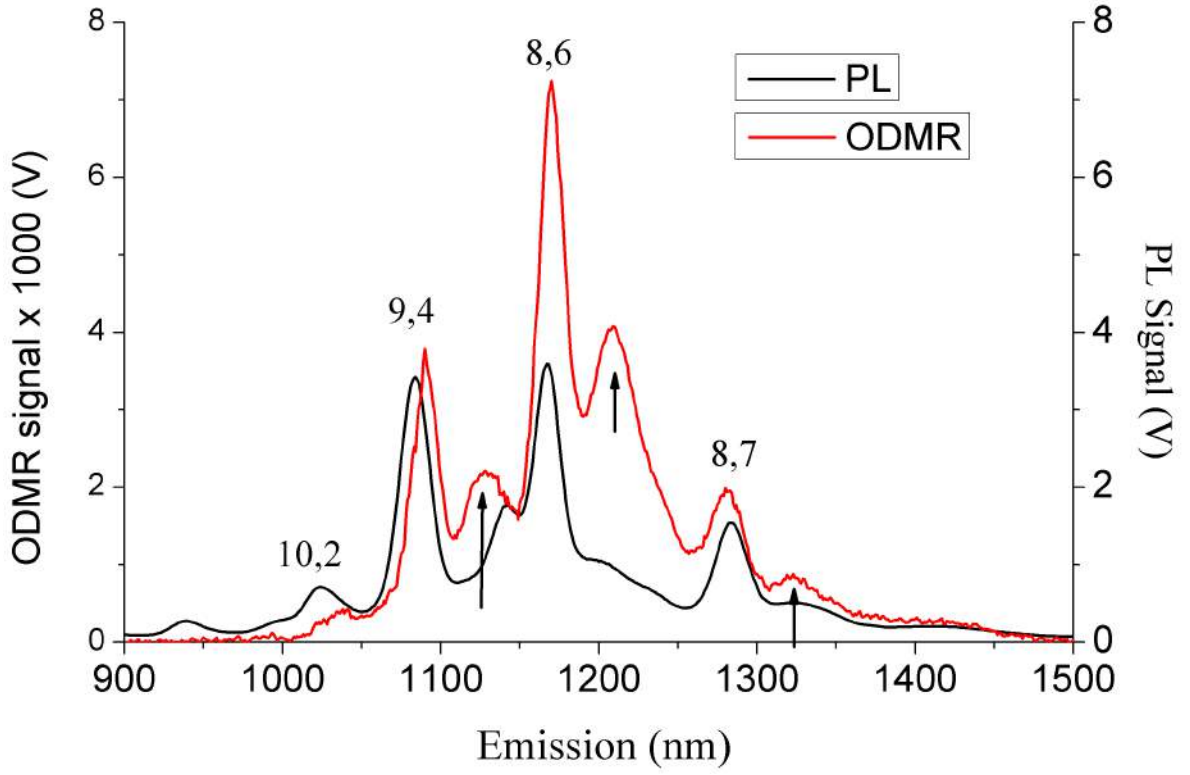

Figure 4.2: Comparing the ODMR emission spectrum of a nanotube sample with a regular PL spectrum.

change in the PL signal due to the microwave irradiation is not dependent on the original signal strength. Instead, it depends on the relations of the populations and lifetimes of the triplet levels to each other. These are different for every nanotube chirality. With these measurements, in the future we can gain some insight into the properties of these triplet levels.

Another interesting fact is the appearance of new peaks in the ODMR spectrum that were not present in the PL. These peaks are always a fixed distance away from the peaks already present in the PL spectrum. The explanation for this is the following: when we apply the microwave irradiation, not only do we change the number of photons generated due to the luminescence cycle but also the number of those generated by phosphorescence. We cannot see the phosphorescence peaks in the original PL spectrum because it is at least three orders of magnitude smaller than the dominant PL peaks. As we discussed in the theoretical introduction into ODMR (2.3), the fluorescence and phosphorescence signal intensities always change equally during the ODMR experiment and this causes the phosphorescence peaks to appear in the ODMR spectrum. If we take a look at the distance between the peaks, in energy domain it is around 40 meV, and literature indeed gives this value for the energy gap between S_1 and T_1 (see: [15]), for the diameter values present in our sample.

4.3 ODMR map

Our next task was to build a 2D representation of the spectra. We took emission spectra with excitations ranging from 712 nm to 802 nm in 6 nm steps. Then, after correcting for the small instability in the laser intensity, we combined those spectra in a single "ODMR map", in a manner similar to a photoluminescence map.

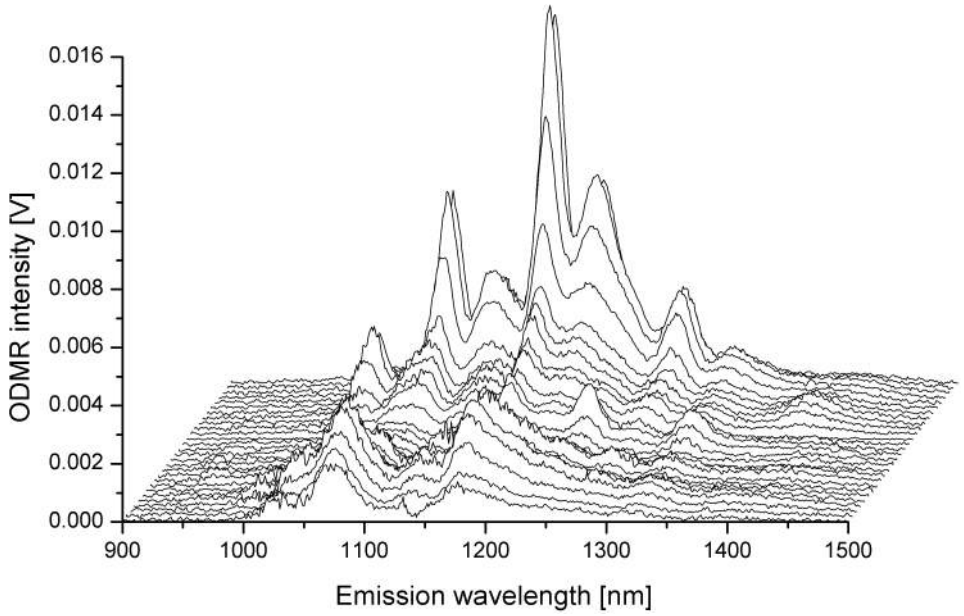

Figure 4.3: An alternative representation of the collected data. The color scale in the following map is directly proportional to the height of the peaks on this one.

As described previously, during the ODMR measurement we also recorded the DC PL signals, so we measured the PL map under the same conditions. The two maps are shown in Figure 4.4.

On the PL map, the spots marked with crosses are the data for the places of the nanotubes from the work of Weisman and Bachilo [16]. The difference of the marks and actual peaks is attributed partly to the temperature difference (reference is taken at 300 K), but a bigger factor is the different surfactant. In [16] the measurements were done using *SDS* (sodium-dodecyl-sulphate) as a surfactant, while we did our measurements using DOC.

The peaks marked with arrows are the phosphorescence sidebands mentioned before. As we noted, they are always a fixed distance (approximately 40 meV [15]) away from the main luminescence peaks. One would intuitively expect the sidebands to be the same strength as the PL peaks. However, this is not the case. We do not yet have a consistent explanation for this effect but we assume that the integrated intensity of the fluorescence and phosphorescence peaks is the same.

The peaks marked with the black star and white stars on the PL map is the result of an the interesting phenomenon we already mentioned in the chapter about photoluminescence. Since the tubes cannot be completely individualized, there exists some cases where a nanotube absorbs a photon to create an exciton, which transfers to a neighboring nanotube, where it recombines, emitting a photon characteristic to that tube. This process creates "ghost" peaks at the crossing of the emission line of the acceptor tube

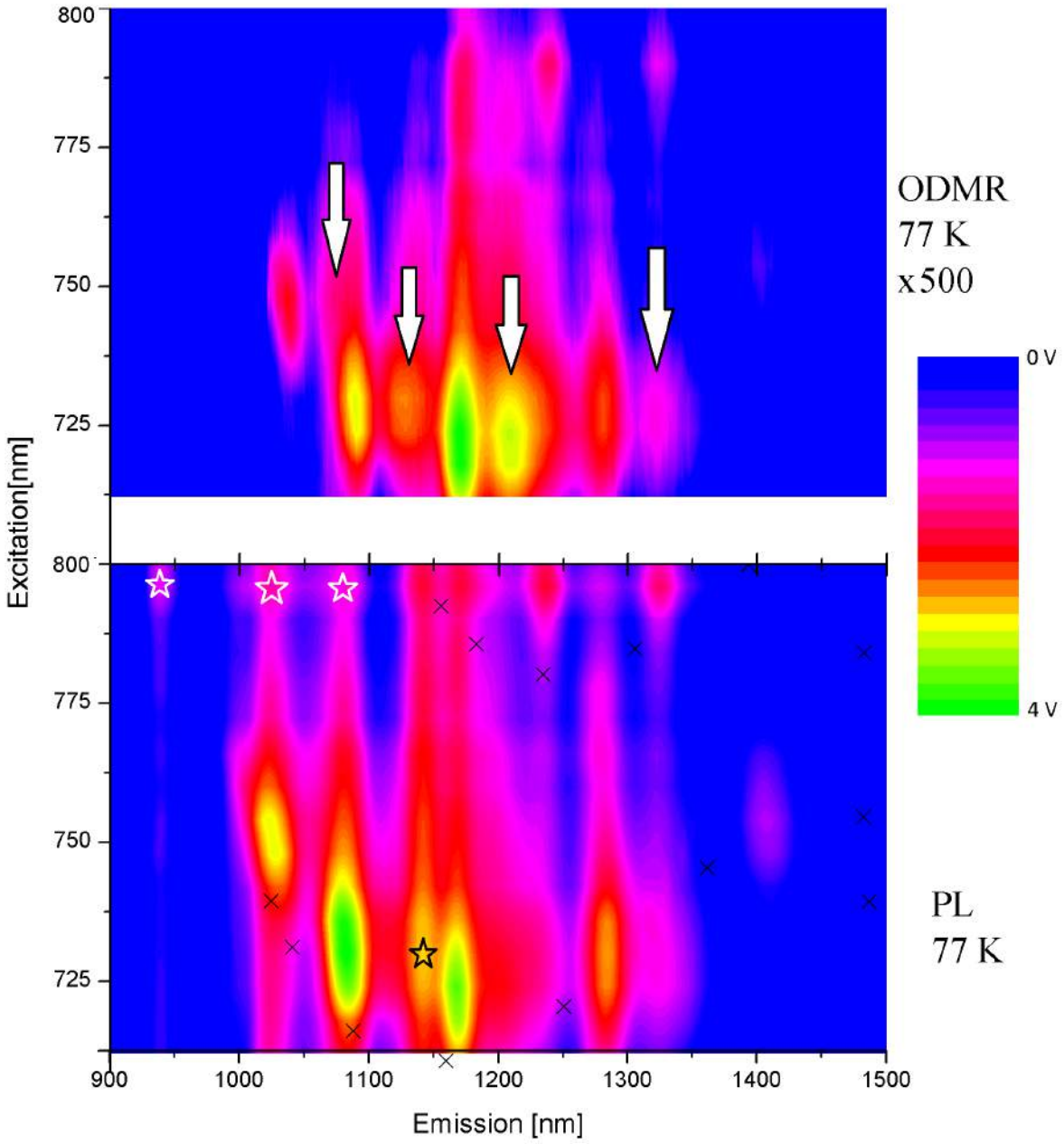

Figure 4.4: Comparing the ODMR emission spectrum of a nanotube sample with a regular PL spectrum.

with the excitation line of the donor tube. The peak marked with the black star is such a "bundle peak" created by exciting the tubes in the (2n+m)=22 nanotube family, then emission by the (9,2) tube.

Peaks marked with white stars originate from a similar process but there is an additional interesting property attributed to them. They are completely missing from the ODMR map, while their emitting tubes still show up on the PL map. (The situation is probably the same with the black star peak but we have no data around its original emission peak to verify it.) To explaing this particular phenomenon, we have to take a look at the Jablonski diagram for the exciton energy transfer between the tubes.

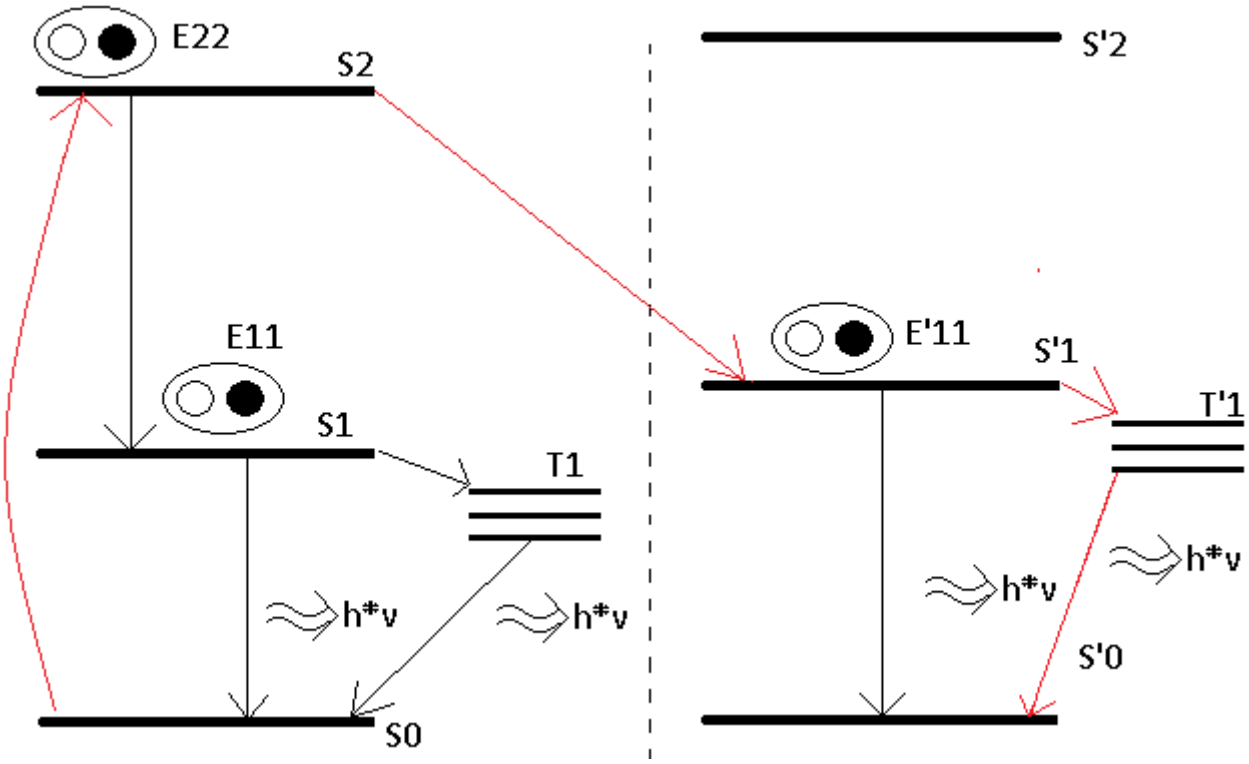

Figure 4.5: Jablonski diagram for a system of two nanotubes. The process corresponding to the emission peaks marked with stars follows the red arrows.

Studying this diagram, we can understand why the peaks are missing from the ODMR spectra. It is because the ODMR signal for those tubes would originate from changing the population of S_1' but only if there is a luminescent cycle also present between S_1' and S_0'. In this case, there is no such cycle, because the emitting tubes are not directly excited by the laser.

In summary, we successfully observed ODMR on SWCNTs and observed the phosphorescence sidebands for the first time. This demonstrates the successful operation of the novel spectrometer. We note, however, that detailed future studies are required to further clarify the details of the ODMR map.

Chapter 5

Conclusions

In this thesis we presented the development and application of a novel, previously nonexistent spectrometer suitable for measuring Optically Detected Magnetic Resonance on heterogeneous carbon nanotube samples. To accomplish this, the spectrometer had to conform to the following specifications:

- tunable laser excitation source
- wavelength-resolved emission detection
- and high-performance light-gathering optical system

which arose from the unique requirements posed by nanotubes.

We described the measurement techniques utilized by us during the development of the spectrometer, and the methods for combining the parts into a single complex system. In regard to this, we described visible and ESR spectrometry techniques, laser systems, and the necessary theoretical background. We also presented our results with the instrumentation and programming of the ODMR spectrometer.

We have used the developed spectrometer to characterize nanotubes using ODMR measurements, which to our knowledge has not been described before in scientific literature. Results acquired by our measurements can be used to further understand nanotubes and their exciton states, especially in regard to photophysics, namely light harvesting and generation.

Bibliography

[1] J. A. Misewich et al. "Electrically Induced Optical Emission from a Carbon Nanotube FET". In: *Science* 300.5620 (2003), pp. 783–786. DOI: 10.1126/science.1081294. eprint: http://www.sciencemag.org/content/300/5620/783.full.pdf. URL: http://www.sciencemag.org/content/300/5620/783.abstract.

[2] Nathaniel M. Gabor et al. "Extremely Efficient Multiple Electron-Hole Pair Generation in Carbon Nanotube Photodiodes". In: *Science* 325.5946 (2009), pp. 1367–1371. DOI: 10.1126/science.1176112. eprint: http://www.sciencemag.org/content/325/5946/1367.full.pdf. URL: http://www.sciencemag.org/content/325/5946/1367.abstract.

[3] J. Shinar. "Optically detected magnetic resonance studies of luminescence-quenching processes in p-conjugated materials and organic light-emitting devices". In: *Laser & Photonics Reviews* 6.6 (2012), pp. 767–786. ISSN: 1863-8899. DOI: 10.1002/lpor.201100026. URL: http://dx.doi.org/10.1002/lpor.201100026.

[4] S. Iijima et al. "Helical microtubules of graphitic carbon". In: *Nature* 354.6348 (1991), pp. 56–58.

[5] Toshinari Ichihashi Sumio Iijima. "Single-shell carbon nanotubes of 1-nm diameter". In: *Nature* 6430 (1993), 603–605. DOI: 10.1038/363603a0. URL: http://www.nature.com/nature/journal/v363/n6430/full/363603a0.html.

[6] D. S. Bethune et al. "Atoms in carbon cages: the structure and properties of endohedral fullerenes". In: *Nature* 6451 (1993), 123–128. DOI: 10.1038/366123a0. URL: http://www.nature.com/nature/journal/v366/n6451/full/366123a0.html.

[7] May 2014. URL: http://www.univie.ac.at/spectroscopy/fks/forschung/ergebnisse/nanotubes.htm.

[8] Juan Yang et al. "Photoluminescence from Exciton Energy Transfer of Single-Walled Carbon Nanotube Bundles Dispersed in Ionic Liquids". In: *The Journal of Physical Chemistry C* 116.41 (2012), pp. 22028–22035. DOI: 10.1021/jp306515a. eprint: http://pubs.acs.org/doi/pdf/10.1021/jp306515a. URL: http://pubs.acs.org/doi/abs/10.1021/jp306515a.

[9] D.A. Skoog, F.J. Holler, and T.A. Nieman. *Principles of instrumental analysis*. Saunders golden sunburst series. Saunders College Pub., 1998. ISBN: 9780030020780. URL: http://books.google.hu/books?id=_7MPAQAAMAAJ.

[10] Michael Kasha. "Characterization of electronic transitions in complex molecules". In: *Discuss. Faraday Soc.* 9 (0 1950), pp. 14–19. DOI: 10.1039/DF9500900014. URL: http://dx.doi.org/10.1039/DF9500900014.

[11] May 2014. URL: http://www.ep4.phy.uni-bayreuth.de/ag_jkoehler/en/research/archive/odmr/index.html.

[12] May 2014. URL: http://felvi.phy.bme.hu/index.php/F%C3%A1jl:Festeklezer.jpg.

[13] May 2014. URL: http://electriciantraining.tpub.com/14183/css/14183_101.htm.

[14] May 2014. URL: http://www.laserfocusworld.com/articles/print/volume-35/issue-5/features/how-to-measure-relative-intensity-noise-in-lasers.html.

[15] Rodrigo B. Capaz et al. "Excitons in carbon nanotubes: Diameter and chirality trends". In: *physica status solidi (b)* 244.11 (2007), pp. 4016–4020. ISSN: 1521-3951. DOI: 10.1002/pssb.200776200. URL: http://dx.doi.org/10.1002/pssb.200776200.

[16] Sergei M. Bachilo et al. "Structure-Assigned Optical Spectra of Single-Walled Carbon Nanotubes". In: *Science* 298.5602 (2002), pp. 2361 –2366. DOI: 10.1126/science.1078727.

Appendix A: Aligning the lasers

The instructions below were written for the dye laser. The only differences are, when applying it for the Ti:Sa laser is that the spots are so weak that it must be dark in the lab, and one has to substitute "crystal" every time "jet" occurs in the text.

1. Set apart the two spots with the lower folding mirror. (Use only the vertical screw.)
2. Mark the spots on a fixed piece of paper.
3. Turn the pump mirror focus, until both spots are well defined. (Usually this means a brighter inner spot, and a halo around it.)
4. By now, the spots have moved. Return them to the marked positions, using only the two pump mirror screws (horizontal and vertical).
5. Realign the two spots with each other, using the vertical screw of the lower folding mirror.
6. If the laser hasn't started yet, start rotating the pump mirror focus systematically, correcting for the spot movements with the two movement screws.
7. At some point, lasing should start.
8. Continue the focus alignment in this direction, with smaller steps. Periodically, also optimize laser power using the other mirrors' screws.
9. You will find a sharp increase in laser power, as you approach the right setting.
10. If the spot on the lower folding mirror is significantly larger than the diameter of the aperture stop on the upper folding mirror, move the lower folding mirror away slightly away from the jet. Repeat this and 9, until you are at the maximum.
11. The laser should always be operating in the TEM00 mode. If this is not the case, laser intensity is significantly smaller than the optimum. To counter this, the most useful technique is to reduce the pump power until the laser is barely working, then optimizing it again. After a few iterations of this, the laser should "snap" into the correct mode, at which point the pump power can be raised again. For the dye laser, it is also important to set the dye pressure to the correct value for the dye used. Also, if nothing else works, check the absorption of the dye jet, if it is over 10%, the dye is too dilute.

Appendix B: A sample from the program code

```
%Public Function cmd_ihr_sweep(cmd, narg, arg(), cmode)
Dim start_n, end_n, inc_n, curr_n As Double
Dim data As Double
Dim D As String
Dim i As Integer
Dim npar As Integer
npar = 5
Dim freq, ampl, phase, tau, sens As Double
Static par(5)
ReDim prompt(5)
Dim status As Variant

Static UseMonoIndex, UseSCDIndex As Integer
Static monoUID, scdUID As String
Dim device_type As Integer

On Error GoTo cmd_ihr_sweep_Error
If break() Then GoTo cmd_ihr_sweep_Error

If narg > npar Then narg = npar
For i = 1 To narg
    par(i) = arg(i)
Next i

If npar <> narg Or cmode = TOEDIT Then
  prompt(1) = "SWEEP START "
  prompt(2) = "SWEEP END "
  prompt(3) = "STEP SIZE "
  prompt(4) = "INTEGRATION TIME"
  prompt(5) = "MEAS. DEVICE"
  status = inputparam(arg(0), npar, prompt(), par(), cmd)
  start_n = Val(par(1))
  end_n = par(2)
  inc_n = par(3)
  SCD1.IntegrationTime = Val(par(4))
  device_type = Val(par(5))
```

```
Else
  start_n = Val(arg(1))
  end_n = arg(2)
  inc_n = arg(3)
  SCD1.IntegrationTime = Val(arg(4))
  device_type = Val(arg(5))
  status = EXEC
End If

Dim time_

If SCD1.IntegrationTime < 0.01 Then SCD1.IntegrationTime = 0.01

If status = EXEC Then
  time_ = Timer

  Mono1.MovetoWavelength (start_n)
  UseSCDIndex = 1 'Val(par(1))
  scdUID = IDARRAY_SCD(UseSCDIndex + 1, 1)
  SCD1.Uniqueid = scdUID
  SCD1.Load
  SCD1.OpenCommunications
  SCD1.initialize
  SCDUpdated = False

  'This part is for the graphical user menu
  header(3) = "ihr_sweep" & " " & par(1) & " " & par(2) & " " &
      par(3) & " " & par(4) & " " & par(5)
  headerupdate

  nbuf = (end_n - start_n) / inc_n + 1
  nch = 4
  For i = 1 To nbuf
    buf(1, i) = start_n + (i - 1) * inc_n
    buf(2, i) = 0: buf(3, i) = 0: buf(4, i) = 0
  Next i
' Xch = 1: Ych = 2: autoscale "xy": plotbuf (1)
  'Conversion is necessary because we want to set in
     wavenumbers, but the spectrometer takes directions in nm

  curr_n = start_n

  GPIBsend LOCKIN, "TSTR 1"                              'manual
     triggering is set, for external trigger
  GPIBsend LOCKIN, "SRAT 14"
  LOCKINread freq, ampl, phase, tau, sens
  'LOCKINset freq, ampl, phase, "0.03", sens
  headerupdate
```

```
'we read in the lockin parameters, and set the proper
   triggering

Do While Mono1.IsBusy
  DoEvents
Loop
i = 1
Do While (curr_n < end_n + 1)

  Mono1.MovetoWavelength (curr_n)
  Do While Mono1.IsBusy
    DoEvents
  Loop

  'If the LI is selected, we make a measurement through GPIB
     protocol
  'GPIBsend LOCKIN, "OUTP ? 2"
  'GPIBenter LOCKIN, D$
  'buf(4, i) = Val(D$)

  'the detector fires an update event which contains the
     measurement, we catch and extract it
  SCD1.DoAcquisition True
  GPIBsend LOCKIN, "OUTP? 1"
  GPIBenter LOCKIN, D$
  buf(3, i) = Val(D$)
  'GPIBsend LOCKIN, "OAUX? 3"
  'GPIBenter LOCKIN, D$
  'buf(2, i) = Val(D$)
  wait 0.001
  Do While SCDUpdated = False
    DoEvents
  Loop
  buf(2, i) = vtData
  SCDUpdated = False
  'this is for the drawing of the spectrum
  'plotpoint (nbuf)

  If (i Mod 10) = 0 Then frmMain!lblStatus = CStr(nbuf) & " /
      " & CStr(i)
  curr_n = curr_n + inc_n
  i = i + 1
Loop
frmMain!lblStatus = frmMain!lblStatus & " elapsed time: " &
   Format(Timer - time_, "#.##") & " sec"

Xch = 1: Ych = 2: P_Color = 0
```

```
  autoscale "xy"
  plotbuf (1)
  Xch = 1: Ych = 3: P_Color = 12
  autoscale "y"
  plotbuf (0)
  Ych = 2

End If
cmd_ihr_sweep = status
Exit Function

cmd_ihr_sweep_Error:
    If Err Then report Error$
    cmd_ihr_sweep = QUIT
    Exit Function
End Function

'this is for catching the fired update event and extracting it

Private Sub SCD1_Update(ByVal updateType As Long, ByVal
   eventInfo As JYSYSTEMLIBLib.IJYEventInfo)
Dim SCDResult As JYSYSTEMLIBLib.IJYResultsObject
Dim SCDData As JYSYSTEMLIBLib.IJYDataObject
Dim data As Variant
Set SCDResult = eventInfo.GetResult
Set SCDData = SCDResult.GetFirstDataObject
    SCDData.GetDataAsArray data
    DoEvents
    vtData = data(0)
SCDUpdated = True 'this flag ensures that we don't catch the
   wrong event

'we get the data as a one-element array, and store the first
   element in a global variable
End Sub
```